**Dissertation**
**submitted to the**
**Combined Faculties for the Natural Sciences and for Mathematics**
**of the Ruperto-Carola University of Heidelberg, Germany**
**for the degree of**
**Doctor of Natural Sciences**

presented by

Diplom-Physiker Andreas Schönle

born in Munich

Oral examination 12.2.2003

# Point Spread Function Engineering
# in
# Fluorescence Spectroscopy

**Point Spread Function Engineering in Fluorescence Spectroscopy:** The combination of high resolution imaging with fluorescence spectroscopy has rendered the microscope into a powerful tool for functional analysis of biological specimens. This thesis explores the potential of techniques, that are usually utilized for PSF-engineering, for the development of new spectroscopical applications. The derivation of a simple integral solution for the Fourier transform of the vectorial PSF lays the foundation for numerical modelling of dynamical, intensity dependent processes in the focal region. Subsequently a theory describing the combination of fluorescence correlation spectroscopy with diffraction limited, periodically modulated detection volumes is derived. This idea leads to the proposal of a 'diffusion and flow microscope' with high spatial resolution. It is readily implemented in a multifocal 4Pi microscope and its potential to extract the parameters of anisotropic diffusion as well as speed and direction of flow inside a fluid is demonstrated in simulations. Finally, experimental evidence is presented that depletion by stimulated emission can be used to identify Förster energy transfer between two molecules inside a sample.

**Manipulation von Punktabbildungsfuntionen in der Fluoreszenzspektroskopie:** Die Synthese von Mikroskopie und Fluoreszenzspektroskopie hat das Mikroskop in ein vielseitiges Werkzeug zur funktionelle Analyse biologischer Systeme verwandelt. In dieser Arbeit wird untersucht, ob und wie kürzlich entwickelte Techniken zur Manipulation von Punktabbildungsfunktionen neue spektroskopische Anwendungen im Mikroskop hervorbringen können. Die Ableitung einer einfachen Integraldarstellung der Fouriertransformation der fokalen Intensitätsverteilung schafft die Grundlage für die numerische Modellierung dynamischer, intensitätsabhängiger Prozesse im Fokus. Als nächstes wird Fluoreszenz-Korrelationsspektroskopie mit Detektionsvolumina, deren beugungsbegrenzte Einhüllende periodisch moduliert ist, theoretisch beschrieben. Darauf aufbauend wird ein 'Diffusions- und Strömungsmikroskop' mit hoher räumlicher Auflösung vorgeschlagen. Sein Aufbau ähnelt dem eines multifokalen 4Pi-Mikroskops und seine Fähigkeit, die Parameter anisotroper Diffusion und die Strömungsrichtung und -geschwindigkeit in einer Flüssigkeit zu bestimmen, wird in simulierten Messungen demonstriert. Zuletzt wird aufgezeigt und experimentell verifiziert, dass Entvölkerung durch stimulierte Emission (stimulated emission depletion) dazu verwendet werden kann, zwischenmolekularen Förster-Energie-Transfer in einer Probe zu identifizieren.

# Contents

4

# Chapter 1

# Introduction

Far field light microscopy is non-invasive and delivers three-dimensional images of life samples. Therefore it is one of the most important tools in the biological sciences. The use of fluorescence as contrast allows functional imaging because the dye can be selectively attached in the nucleus, cell membrane, to certain molecules or even specific sites on macromolecules. At the same time it allows for the combination of imaging with methods from fluorescence spectroscopy. By measuring the spectral and temporal form of the signal in addition to its intensity, information about the chemical and physical environment of the dye can be assessed. For example, fluorescence correlation spectroscopy (FCS)[1] delivers statistical information about movement and reactions of stained units which are too small and too dense to be individually resolved. Distances can be measured by monitoring resonant energy transfer between two dye molecules revealing structural information[2], and identifying reaction partners.[3]

Owing to the wave nature of light the pass-band of a microscope is cut off at high spatial frequencies, and the resolution of far field microscopy is therefore fundamentally limited. This diffraction barrier, first postulated by Abbe[4] had long been considered an unalterable fact. However, since the confocal laser scanning microscope enabled three-dimensional imaging and widened the lateral pass-band the problem has received renewed attention and the field of point-spread function engineering emerged. Several methods were found how the shape and, more importantly, the size of the effective detection volume of a microscope can be influenced.

A number of approaches is based on diffraction itself. The form of the focal intensity distribution can be shaped by specific aberrations of the wavefront using a pupil filter.[5] However, a significant resolution increase can not be achieved in

lateral or axial direction without producing large sidelobes and pupil filters are mainly useful in combination with other techniques.[6, 7] By interfering two counter-propagating beams an axial pattern is produced in the focus of a 4Pi microscope. The aperture is effectively doubled and typically a more than 4-fold improvement in axial resolution is achieved.[8] Despite this success, the resolution limit is still governed by diffraction in such a microscope. It is only by combining the aimed reshaping of focal intensity distributions with a spectroscopical method that resolution becomes independent of diffraction. The idea is to establish a nonlinear dependence of the signal on the intensity distribution. Several methods based on this approach have been proposed[9, 10, 11] and in practice stimulated emission depletion (STED) microscopy increased the resolution to less than 100nm, far beyond the Abbe limit. [12, 13, 14]

On the other hand, methods originally aiming at the improvement of resolution have been most useful in purely spectroscopical applications: The small detection volume and low background of a confocal detection scheme is one of the prerequisites for single molecule detection, currently one of the most active fields of research.

The goal of this work was to analyze whether the recently developed and established techniques in STED and 4Pi microscopy can also provide feedback to spectroscopical applications. For this purpose the following problems were addressed.

**1)** The foundation for theoretical modelling of dynamical, intensity dependent processes in the focal region is laid by developing a method to calculate the Fourier transform of the vectorial PSF with little numerical effort. As an application the temperature rise due to linear absorption by water is calculated.

**2)** The prospects of combining 4Pi microscopy with FCS are analyzed. It is found that by comparing correlation curves recorded with a standard, confocal and a 4Pi detection volume, information about the movement of fluorescent units can be separated from fluctuations due to internal dynamics or reactions. Because the interference pattern has a well-defined orientation, directional information in anisotropic samples is also obtained. Therefore a method to produce patterns in lateral, axial and diagonal directions is proposed and a theory of FCS in anisotropic media is developed allowing for arbitrary periodic modulations of

the detection volume. Simulations show that all parameters of the anisotropic model can be extracted from a small number of correlation measurements with various pattern orientations.

**3)** When measuring fluorescence resonant energy transfer (FRET) in complex environments by comparing donor and acceptor fluorescence, contributions from uncoupled donor molecules are a source of uncertainty. This problem could be overcome by measuring the excitation rate of the acceptor directly. However, time resolved measurements in the time or frequency domain, which are currently used inside microscopes have limited temporal resolution and cannot assess high transfer rates. Therefore the possibility of using a STED beam to monitor the excited state of the acceptor is explored. Experiments on a model system show that energy transfer can be identified using this technique.

# Chapter 2

# Transfer Functions

Large-angle focusing systems, such as objective lenses or high angle mirrors are of great scientific interest because they are used whenever high spatial resolution is required. Importantly, their imaging properties are determined by the spatial distribution of quantities that depend on products of the vector components of the electromagnetic field in image space. For example, the modulus squared of the electric field is proportional to the electrical energy density, which in turn determines the intensity point spread function (I-PSF) for incoherent imaging.

Transfer functions describe which spatial frequencies are transmitted by an optical system. They play an important role in the analysis of three dimensional image formation in the Fourier domain because the finite pass-band and damping of high spatial frequencies are the reason for limited spatial resolution.[15, 16] In addition, transfer functions are useful tools for the modelling and quantitative analysis of photophysical processes in the focal spot, because the differential equations involved are often solved in inverse space.

For incoherent imaging the 3D-optical transfer function (OTF) is the Fourier transform of the I-PSF. It was introduced by Frieden[17] and its paraxial approximation was derived in the same publication. However, for lenses of high numerical aperture this approximation is not fully valid and the computation of the OTF for conventional, confocal, and multiphoton microscopy has since been an active field of research. The derivation of an analytical expression allowing for fast and efficient calculation of the scalar OTF proved especially useful in numerical calculations.[18, 19]

At large focusing angles the vectorial nature of the electromagnetic field becomes increasingly significant and the accuracy of the scalar description is compromised.[20, 21, 22] More importantly many applications involve imaging of anisotropic samples such

as a distribution of oriented dipoles in single molecule experiments. The scalar theory cannot be applied in such cases and an efficient way to calculate the vectorial OTF becomes a necessity.

Richards and Wolf have given an integral representation for the electromagnetic field in the focus.[23] In principle one could use these results to numerically determine the spatial distribution of the PSF, or of any other observable depending on the fields, numerically and subsequently Fourier transform the results. However the computation in two steps is extensive and controlling the numerical error is difficult. If the transform is not required simultaneously at all points of an equidistant grid this method is particularly inadequate, because FFT algorithms can not be used efficiently.

Alternatively, the OTF can be expressed as the correlation of the vector components of the pupil function. In two dimensions numerical correlation yields the 2D OTF on a discrete grid[24], but in 3D this approach fails because the pupil functions are non-zero on spherical shells only. However, the correlation can be written as a single line integral along the circular intersection of the two spheres. Frieden used this method to derive the OTF in the paraxial approximation where the spheres are replaced by parabolic surfaces.[17] For high angle focusing systems this approach was successfully used to derive an analytical expression of the scalar OTF[18] under the assumption of cylindrical symmetry. Importantly, the transverse nature of light breaks this symmetry so that a more general formalism is needed in the vectorial theory. The formalism developed here allows for arbitrary pupil functions and will be used to derive a line integral representation of the Fourier transform of an arbitrary product of two vector components of the electromagnetic field and its complex conjugate. The results are used to calculate the vectorial OTF for both a single lens and the case of interfering foci in a 4Pi microscope. Due to the general form of the pupil function it is possible to extend the theory to describe spherical aberrations induced by focusing through an interface of two media with mismatched refractive indices.

As a first application of the newly found integrals focal heating is addressed. The problem can now be modelled taking into account the true three-dimensional profile of the vectorial PSF and an upper bound is found for the temperature increase due to linear absorption by water.

## 2.1  The Vectorial Optical Transfer Function

In fluorescence imaging the excitation probability is proportional to the electric energy density and the excitation OTF is given by its Fourier transform. It can be written as the sum of its vector components, which correspond to the contribution of the three polarization directions

$$C = \mathcal{F}[e_x e_x^*] + \mathcal{F}[e_y e_y^*] + \mathcal{F}[e_z e_z^*] = C_x + C_y + C_z \tag{2.1}$$

We will express the components of the electric field as inverse Fourier transforms of spherical shells. The convolution theorem can then be applied to equation (2.1) and the OTF is given by correlations of these shells which we will express as a line integral.

Let $(r, \theta, \phi)$ be dimensionless spherical coordinates originating at the focal point and normalized with the wave vector $2\pi/\lambda$. The spherical inverse coordinates are $(k, \vartheta, \varphi)$, and $\alpha$ is the half aperture angle of the lens. Using the same assumptions as Richards and Wolf[23] we write each component of the focal field as the Fourier transform of the related component of the vectorial 3D pupil function.

$$f(r, \theta, \phi) = iA\,\mathcal{F}\big[P(\vartheta, \varphi)\,a_f(\vartheta, \varphi)\,\delta(k-1)\big]/\pi \tag{2.2}$$

The scalar pupil function $P(\vartheta, \varphi)$ describes a relative amplitude and phase common to all components of the electromagnetic fields throughout the spherical exit pupil and vanishes for $\vartheta > \alpha$. $A$ is a scaling factor and the functions $a_f(\vartheta, \varphi)$ are scalar strength factors. For the individual vector components of the electric field they are[23]

$$a_{e_x} = -\cos\vartheta\cos^2\varphi - \sin^2\varphi \tag{2.3a}$$

$$a_{e_y} = \cos\varphi\sin\varphi\,(1 - \cos\vartheta) \tag{2.3b}$$

$$a_{e_z} = \sin\vartheta\cos\varphi \tag{2.3c}$$

In the case of mismatched refractive indices these strength factors will have to be modified due to refraction at the interface. Defining

$$A_f(\mathbf{k}) = iA\,P(\pi - \vartheta, \pi + \varphi)\,a_f(\pi - \vartheta, \pi + \varphi)/\pi \tag{2.4}$$

we rewrite (2.2) as an inverse Fourier transform

$$f = \mathcal{F}^{-1}\big[A_f\,\delta(k-1)\big] \tag{2.5}$$

Equation (2.1) contains only Fourier transforms of a field component multiplied with its own complex conjugate. We keep our formalism more general and consider Fourier transforms of products of two arbitrary field components $f$ and $g$. Using the convolution theorem and (2.5) we can write them as the correlation of two weighted spherical shells

$$\mathcal{F}[f^*g](\mathbf{k}) = (2\pi)^3 \int d^3k' A_f^*(\mathbf{k}') \delta(k'-1) A_g(\mathbf{k}+\mathbf{k}') \delta(|\mathbf{k}+\mathbf{k}'|-1) \quad (2.6)$$

Next we introduce Cartesian coordinates in inverse space and a new coordinate system denoted by double prime coordinates as shown in figure 2.1. The transformation is described by an orthogonal matrix:

$$\mathbf{k}' = \begin{bmatrix} \cos\vartheta\cos\varphi & -\sin\varphi & \sin\vartheta\cos\varphi \\ \cos\vartheta\sin\varphi & \cos\varphi & \sin\vartheta\sin\varphi \\ -\sin\vartheta & 0 & \cos\vartheta \end{bmatrix} \mathbf{k}'' \quad (2.7)$$

With $\mathbf{k}_1 = \mathbf{k}'$ and $\mathbf{k}_2 = \mathbf{k}+\mathbf{k}'$ equation (2.6) reads

$$\mathcal{F}[f^*g](\mathbf{k}) = (2\pi)^3 \int d^3k'' k''^2 d\cos\vartheta'' d\varphi'' A_f^*(\mathbf{k}_1) A_g(\mathbf{k}_2)$$
$$\times \delta(k'') \delta\left([(k+k''\cos\vartheta'')^2 + (k''\sin\vartheta'')^2]^{1/2} - 1\right) \quad (2.8)$$

and after radial integration and simplification of the delta function's argument we obtain

$$\mathcal{F}[f^*g](\mathbf{k}) = (2\pi)^3 \int d\cos\vartheta'' d\varphi'' A_f^*(\mathbf{k}_1) A_g(\mathbf{k}_2)$$
$$\times \delta\left([k^2 + 2k\cos\vartheta + 1]^{1/2} - 1\right)\Bigg|_{k''=1} \quad (2.9)$$

Azimuthal integration finally yields

$$\mathcal{F}[f^*g](\mathbf{k}) = (2\pi)^3 \int d\varphi'' A_f^*(\mathbf{k}_1) A_g(\mathbf{k}_2) /k \Bigg|_{\cos\vartheta''=-k/2, k''=1} \quad (2.10)$$

which indeed is a line integral along a circle of radius $r_0 = [1-k^2/4]^{1/2}$. If we define $a = r_0 \cos\vartheta\cos\varphi''$, $b = (k\sin\vartheta)/2$ and $d = r_0 \sin\phi''$, we can use (2.7) to calculate the Cartesian components $(m,n,s)$ of $\mathbf{k}_1$ and $\mathbf{k}_2$

$$m_{1/2} = (a \mp b)\cos\varphi - d\sin\varphi \quad (2.11a)$$
$$n_{1/2} = (a \mp b)\sin\varphi + d\cos\varphi \quad (2.11b)$$
$$s_{1/2} = -r_0 \sin\vartheta\cos\varphi'' \mp (k\cos\vartheta)/2 \quad (2.11c)$$

Note that the functions $A_f$ only depend on the sine and cosine functions of the spherical angles. It is straightforward to express them as functions of the Cartesian components in equation (2.11) using the following relations:

$$\cos(\pi + \varphi_{1/2}) = -m_{1/2}/(1 - s_{1/2}^2)^{1/2} \tag{2.12a}$$

$$\sin(\pi + \varphi_{1/2}) = -n_{1/2}/(1 - s_{1/2}^2)^{1/2} \tag{2.12b}$$

$$\cos(\pi - \vartheta_{1/2}) = -s_{1/2} \tag{2.12c}$$

$$\sin(\pi - \vartheta_{1/2}) = (1 - s_{1/2}^2)^{1/2} \tag{2.12d}$$

We defined the pupil functions to be non-zero only for $\vartheta \leq \alpha$. The integration range the integration range in (2.10) is thus defined by $-s_{1/2} \geq \cos\alpha$ yielding

$$0 \leq |\varphi''| \leq \beta_1 = \arccos\left[(2\cos\alpha + k\,|\cos\vartheta|)\,/\,(2r_0\sin\vartheta)\right] \tag{2.13}$$

and $\beta_1 = 0$ if the argument of the inverse cosine is larger than unity. For arbitrary pupil functions the integral in (2.10) can now be solved numerically.

If we restrict ourselves to cylindrically symmetric scalar pupil functions, it is possible to extract the dependence on the polar angle from the integrals which reduces numerical effort significantly in most applications. We use (2.4), (2.11) and (2.12) to rewrite the integral in equation (2.10). Due to the symmetric integration range, we can remove all asymmetric terms from the integrand and restrict the integration range to positive $\varphi''$. In a second step one can use simple trigonometry to rewrite the angular dependence in terms of $\cos 2\varphi$ and $\cos 4\varphi$, yielding

$$C_x = 16\pi\left(I_0 + I_1\cos 2\varphi + I_2\cos 4\varphi\right)/k \tag{2.14a}$$

$$C_y = 16\pi\left(I_3 - I_2\cos 4\varphi\right)/k \tag{2.14b}$$

$$C_z = 16\pi\left(I_4 + I_5\cos 2\varphi\right)/k \tag{2.14c}$$

with

$$I_i = \int_0^{\beta_1} P^*\left(\pi - \vartheta_1\right)P\left(\pi - \vartheta_2\right)J_i\,d\varphi'' \tag{2.15}$$

If we define the variables $S_{2/1} = s_{1/2}/(1 - s_{1/2})$ and $S_3 = (1 - s_1)^{-1}(1 - s_2)^{-1}$ the integrands evaluate to

$$J_0 = S_3\left[3J_4^2 + b^2d^2\right]/2 - L + s_1s_2 \tag{2.16a}$$

$$J_1 = S_3\left[d^4 - (a^2 - b^2)^2\right]/2 + L - (S_1 + S_2)d^2 \tag{2.16b}$$

$$J_2 = S_3\left[J_5^2 - a^2d^2\right]/2 \tag{2.16c}$$

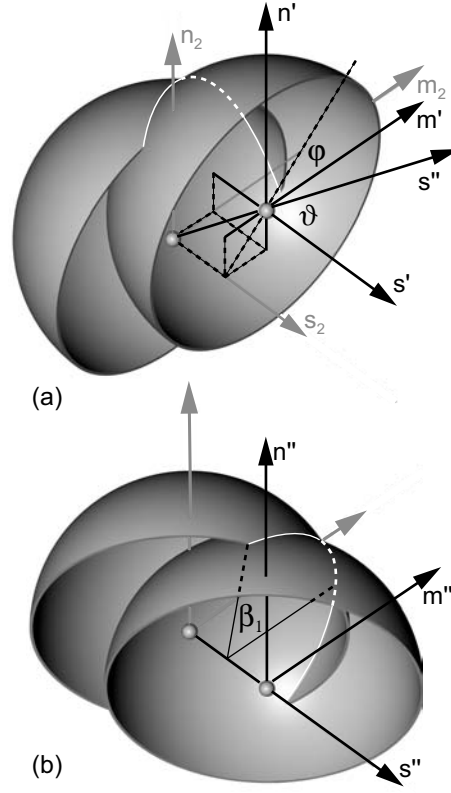$$J_3 = S_3\left[J_4^2 - b^2d^2\right]/2 \tag{2.16d}$$

Figure 2.1: *3D correlation of two spherical shells. The figure illustrates the coordinate systems and the angles of the rotation matrix used in the text. The center of the first sphere is located at the origin of the primed coordinate system while the second center is at $-\mathbf{k}$. Their circular intersection is shown as a white line. The new, double primed coordinate system is chosen such that the centers of both spheres are on the new $s''$-axis. This is accomplished by rotating the coordinate system first by an angle $\varphi$ around the $s'$ axis and then by an angle $\vartheta$ around the $n'$ axis as illustrated in (a). The intersection is now in the plane of constant $s''$ and centered about the $s''$-axis as shown in (b).*

with

$$J_4 = \left(a^2 - b^2 + d^2\right)/2 \tag{2.16e}$$

$$J_5 = \left(a^2 - b^2 - d^2\right)/2 \tag{2.16f}$$

and

$$L = S_1\left[(a-b)^2 + d^2\right]/2 + S_2\left[(a+b)^2 + d^2\right]/2 \tag{2.16g}$$

The results of the scalar theory are reproduced if we use the correlation of $A_f(\mathbf{k}) =$

$iA\,P(\pi - \vartheta)/\pi$ in equation (2.10), yielding

$$C\left(k, \vartheta\right) = 16\pi A^2 \int_0^{\beta_1} d\varphi'' P^*\left(\pi - \vartheta_1\right) P\left(\pi - \vartheta_2\right)/k \qquad (2.17)$$

We now change to cylindrical optical coordinates, defined by $v = r\sin\alpha\sin\theta$, $u = 4r\sin^2\left(\alpha/2\right)\cos\theta$ and the polar angle $\phi$. When using the inverse coordinate system

$$\left(l = k\sin\vartheta/\sin\alpha, s = k\cos\vartheta/4\sin^2\left(\alpha/2\right), \varphi\right) \qquad (2.18)$$

we have to scale the result by a factor $4\sin^2\alpha\sin^2\left(\alpha/2\right)$ due to the coordinate transformation. It then satisfies the scaling condition

$$\mathcal{F}^{-1}\!\left[C\right]\left(\mathbf{0}\right) = \left(2\pi\right)^{-3}\int d\phi\,dl\,ds\,C(l, s, \phi) = \mathbf{e}^t(\mathbf{0})\,\mathbf{e}^*(\mathbf{0}) \qquad (2.19)$$

In addition one can choose the scaling factor A in such a way, that the Fourier back-transform of the OTF at the origin, $\mathbf{e}^t(\mathbf{0})\mathbf{e}^*(\mathbf{0})$, becomes unity. The choice depends on the pupil function. For aplanatic, uniform and parabolic apodization we have $P_{\mathrm{a}}\left(\vartheta\right) = \left(\cos\vartheta\right)^{1/2}$, $P_{\mathrm{u}}\left(\vartheta\right) = 1$, and $P_{\mathrm{p}}\left(\vartheta\right) = 2/\left(1 + \cos\vartheta\right)$, respectively. The corresponding A's can be determined by evaluating equation (2.2) using the integrals derived by Richards and Wolf and subsequent normalization.

$$A_{\mathrm{a}} = \left(\tfrac{16}{15} - \tfrac{3}{2}\cos^{\frac{3}{2}}\alpha - \tfrac{2}{5}\cos^{\frac{5}{2}}\alpha\right)^{-1} \qquad (2.20a)$$

$$A_{\mathrm{u}} = \left(\tfrac{3}{2} - \cos\alpha - \tfrac{1}{2}\cos^2\alpha\right)^{-1} \qquad (2.20b)$$

$$A_{\mathrm{p}} = \left(2 - 2\cos\alpha\right)^{-1} \qquad (2.20c)$$

After implementing our integrals we checked their validity by Fourier transforming the components of the OTF and comparing the result to the vectorial PSF. For randomly polarized illumination, equation (2.14) must be averaged over the polar angle and only $I_0$, $I_3$ and $I_4$ need to be solved. Additionally, transition moments oriented along the x- and y-axis are now imaged identically and we are left with an axial and a lateral component of the OTF as presented in figure 2.2.

## 2.2 Mismatched Refractive Indices

Focusing through an interface of two isotropic, homogeneous media with different refractive indices results in spherical aberrations. This problem is frequently encountered in microscopy, e.g. when imaging a sample mounted in glycerol using an oil immersion lens, and several approaches exist to calculate the resultant electromagnetic field in the focal region.[25, 26] Starting from these results we shall
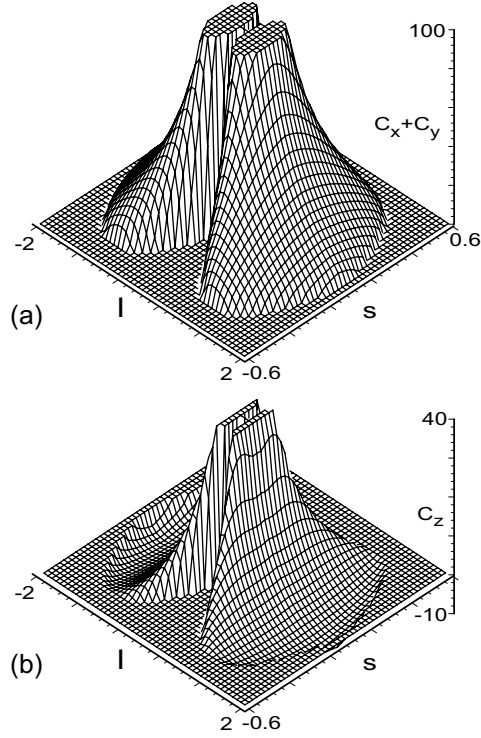
**Figure 2.2:** *Lateral (a) and axial (b) component of the vectorial OTF for randomly polarized illumination using a lens with half aperture angle $\alpha = 1.1$. The axial component corresponds to imaging a molecular transition moment oriented along the optic axis while the lateral counterpart applies to an orientation parallel to the focal plane.*

write the focal field as an inverse Fourier transform of a modified vectorial pupil function and apply our formalism. We assume that the light emerges from the lens as a perfect spherical wave that initially propagates in medium 1. At a distance $\Delta$ from the Gaussian focus it is refracted by a planar interface between medium 1 and medium 2. Let $n_1$ and $n_2$ be the refractive indices of the media and $(r, \theta, \phi)$ be spherical coordinates normalized with the wave vector in medium 2 and centered at the Gaussian focus. We write again $(k, \vartheta, \varphi)$ for the inverse coordinates and define the angle $\bar{\vartheta} = \arcsin(n_2 \sin \vartheta / n_1)$. Török and coworkers extended the theory of Richard and Wolf to represent the field in medium 2 as a superposition of plane waves.[26] In their solution for the fields we change the integration variable from $\bar{\vartheta}$ to $\vartheta$. The Jacobian of this transformation is

$$n_2^2 \cos \vartheta / (n_1^2 \cos \bar{\vartheta}) = n_2 \gamma / n_1 \tag{2.21}$$
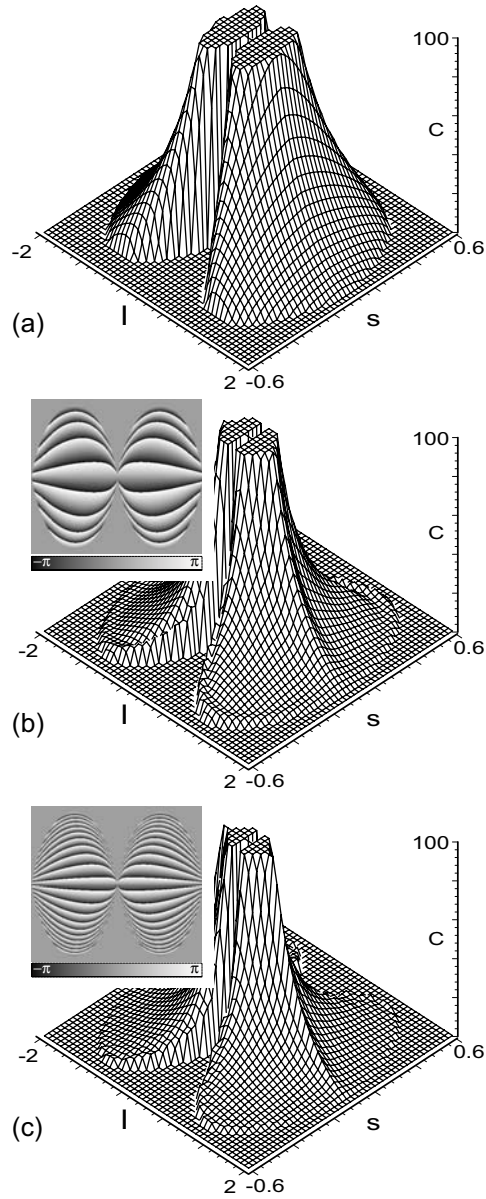
**Figure 2.3:** *Modulus of the vectorial OTF (a) for an unaberrated system and (b),(c) when focusing into 80% glycerol ($n_2 = 1.45$) with an oil ($n_1 = 1.52$) immersion lens The Gaussian focus was assumed at (b) 20µm and (c) 50µm from the interface and the half aperture angle was $\alpha = 1.1$. For the aberrated cases the phase is shown in the insets.*

where we defined the function $\gamma$. The integrals can now be identified as Fourier transforms in the form of equation (2.2) but with modified strength factors and

a modified scalar pupil function. The strength vectors are

$$a_{e_x} = -\tau_{\mathrm{p}} \cos\vartheta \cos^2\varphi - \tau_{\mathrm{s}} \sin^2\varphi \tag{2.22a}$$

$$a_{e_y} = \cos\varphi \sin\varphi \left(\tau_{\mathrm{s}} - \tau_{\mathrm{p}} \cos\vartheta\right) \tag{2.22b}$$

$$a_{e_z} = \tau_{\mathrm{p}} \sin\vartheta \cos\varphi \tag{2.22c}$$

The Fresnel coefficients, $\tau_s$ and $\tau_p$, are functions of $\vartheta$ and given by

$$\tau_{\mathrm{s}} = 2\sin\vartheta \cos\bar{\vartheta} / \sin(\bar{\vartheta} + \vartheta) = 2(1+\gamma) \tag{2.23a}$$

$$\tau_{\mathrm{p}} = \tau_{\mathrm{s}} / \cos(\bar{\vartheta} - \vartheta) = \tau_{\mathrm{s}} / \left[n_2 + n_2 \cos^2\vartheta(\gamma^{-1} - 1)\right] \tag{2.23b}$$

The new pupil function is

$$P(\vartheta, \varphi) = n_2\gamma/n_1 \cdot \exp\left[-i\Delta(\gamma^{-1} - 1)\cos(\vartheta)\right] \bar{P}(\bar{\vartheta}, \varphi) \tag{2.24}$$

where $\bar{P}(\bar{\vartheta}, \varphi)$ is the pupil function in the absence of refraction. The new pupil function is nonzero only for $\vartheta \leq \alpha_2$ with the effective aperture angle $\alpha_2 = \arcsin(n_2 \sin\alpha/n_1)$. However, if $\sin\alpha \geq n_2/n_1$ total internal reflection occurs for the large incident angles and we have $\alpha_2 = \pi/2$. In order to calculate the OTF we rewrite the trigonometric functions of the azimuthal and polar angles in terms of $\varphi''$ using equations (2.11), (2.12) and solve the integral in (2.10). Its range is still determined by equation (2.13) but $\alpha$ has to be replaced by $\alpha_2$.

If we assume a cylindrically symmetric pupil function the calculations are very similar to those for an unaberrated system. Using the same definitions as in equation (2.1) and (2.14) the result is again given by equation (2.15) but with modified integrands $J_i$. If we redefine the factors

$$S_{1/2} = \tau_{\mathrm{p},2/1} s_{2/1}\left(\tau_{\mathrm{s},1/2} + \tau_{\mathrm{p},1/2} s_{1/2}\right)/\left(1 - s_{1/2}^2\right) \tag{2.25a}$$

$$S_3 = S_1 S_2 / \left(s_1 s_2 \tau\right) \tag{2.25b}$$

where $\tau = \tau_{\mathrm{p},1}\tau_{\mathrm{p},2}$, the integrands take almost the same form as before:

$$J_0 = S_3\left[3J_4^2/\tau^2 + b^2 d^2\right]/2 - L + s_1 s_2 \tau \tag{2.25c}$$

$$J_1 = S_3\left[d^4 - (a^2 - b^2)^2\right]/2 + L - (S_1 + S_2)d^2 \tag{2.25d}$$

$$J_2 = S_3\left[J_5^2/\tau^2 - a^2 d^2\right]/2 \tag{2.25e}$$

$$J_3 = S_3\left[J_4^2/\tau^2 - b^2 d^2\right]/2 \tag{2.25f}$$

with

$$J_4 = (a^2 - b^2 + d^2)/2 \tag{2.25g}$$

$$J_5 = (a^2 - b^2 - d^2)/2 \tag{2.25h}$$

and

$$L = S_1[(a-b)^2 + d^2]/2 + S_2[(a+b)^2 + d^2]/2 \tag{2.25i}$$

For identical refractive indices in both media ($n_1/n_2 \to 1$) the Fresnel coefficients become unity and equation (2.16) is reproduced. We introduce the same inverse optical coordinates from (2.18) and therefore have to multiply the result by the identical scaling factor $4 \sin^2 \alpha \sin^2 (\alpha/2)$. The pre-factor $A$ is given by equation (2.20). In figure 2.3 we evaluated the OTF for the common situation of focusing from oil into glycerol. The results for two different focusing depths are shown in (b) and (c) and compared to the vectorial OTF without aberrations in (a). With increasing focusing depths the OTF is suppressed at high axial frequencies, corresponding to a loss in axial resolution. The oscillation of its phase along the inverse optic axis corresponds to a shift of the main maximum of the PSF induced by refraction and the contortion of the resulting pattern is due to spherical aberrations. The shift of the maximum depends on the focusing depth and the aperture angle $\alpha$ and has to be determined numerically. When the light is not focused deeper than several tens of micrometers into the second material, the focal shift is proportional to the depth. In the paraxial approximation, that is for small aperture angles, it is given by $\Delta(n_2/n_1 - 1)$ as predicted by geometrical optics.[27, 28]

## 2.3   Transfer Functions of 4Pi Microscopes

In a 4Pi microscope, two beams which are focused by opposing objective lenses, form an interference pattern. Let the electric fields of the lenses be given by $\mathbf{e}_1(\mathbf{r})$ and $\mathbf{e}_2(\mathbf{r})$ where $\mathbf{r}$ originates at their respective Gaussian focus points. In the aberrated case the focusing depths of the lenses differ due to axial scanning of the sample. They are usually chosen in such a way, that both fields have their maximum amplitude in the same point, which we will define to be the origin. The Gaussian focus points of the two lenses are then located at positions $\mathbf{d}_{1,2} = d_{1,2}\hat{\mathbf{z}}$, which depend on the focusing depths and the aperture angle. The electric field is now given by

$$\mathbf{e}_{4\text{Pi}}(\mathbf{r}) = \mathbf{e}_1(\mathbf{r} - \mathbf{d_1}) + \mathbf{M}^{-1}\mathbf{e}_2(\mathbf{M}\mathbf{r} - \mathbf{M}\mathbf{d_2})\exp(i\phi) \tag{2.26}$$

where $\phi$ is the relative phase of the beams and the diagonal matrix depends on the geometry of the interferometer. For a triangular setup we have

$$\mathbf{M} = \begin{bmatrix} 1 & 0 & 0 \\ 0 & 1 & 0 \\ 0 & 0 & -1 \end{bmatrix} \tag{2.27}$$

The OTF is the Fourier transform of the modulus of (2.26) and consists of the sum of the single lens OTFs and an additional addend accounting for the interference of the fields described by the new function $\mathcal{C}(\mathbf{k})$.

$$C_{4\mathrm{Pi}}(\mathbf{k}) = C(\mathbf{k}) \exp(i\mathbf{d}_1^t \mathbf{k}) + C(M\mathbf{k}) \exp(i\mathbf{d}_2^t \mathbf{k})$$
$$+ \mathcal{C}(\mathbf{k}) \exp(i\phi) + \mathcal{C}(-\mathbf{k})^* \exp(-i\phi) \quad (2.28)$$

The phase factors in the first line originate from the relocation of the origin in (2.26). The function $\mathcal{C}$ is given by

$$\mathcal{C}(\mathbf{k}) = \mathcal{F}\Big[\mathbf{e}_1^{*t}(\mathbf{r} - \mathbf{d}_1)\mathbf{M}\mathbf{e}_2(\mathbf{M}\mathbf{r} - \mathbf{M}\mathbf{d}_2)\Big](\mathbf{k})$$
$$= \Big(\mathcal{F}[\mathbf{e}_1](\mathbf{k}) \exp(i\mathbf{d}_1^t \mathbf{k})\Big)^* \tilde{\otimes} \Big(\mathbf{M}\mathcal{F}[\mathbf{e}_2](M\mathbf{k}) \exp(i\mathbf{d}_2^t \mathbf{k})\Big) \quad (2.29)$$

where the Fourier transform and convolution applies to each vector component of the field separately and we used the fact that $\mathbf{M}$ is always diagonal. The convolution theorem has been applied in order to find the expression in the second line and $\tilde{\otimes}$ symbolizes the correlation of both factors. The Fourier transforms of the field components are given by the functions $A_f$ and therefore we can apply our formalism from the previous section. The integral (2.10) now reads

$$\mathcal{F}[f^* g](\mathbf{k}) = (2\pi)^3 \int d\varphi'' \exp(-i\mathbf{d}_1^t \mathbf{k}_1) \exp(i\mathbf{d}_2^t \mathbf{k}_2)$$
$$A_f^*(\mathbf{k}_1) A_g(\mathbf{M}\mathbf{k}_2)/k \Big|_{\cos\vartheta'' = -k/2, k''=1} \quad (2.30)$$

where $f$ and $g$ are vector components of $\mathbf{e_1}$ and $\mathbf{e_2}$ and in the absence of aberrations $f = g$. Due to the multiplication of the argument with the matrix $\mathbf{M}$ the integration range changes. As before $-s_1 \geq \cos\alpha$ but for the second sphere the minus sign disappears and $s_2 \geq \cos\alpha$. Consequently we have

$$\beta_2 \leq |\phi''| \leq \pi - \beta_2$$
$$\beta_2 = \arccos\left[(k\cos\vartheta - 2\cos\alpha_2)/(2r_0 \sin\vartheta)\right] \quad (2.31)$$

If the argument of the inverse cosine is larger than 1 or smaller than zero, we have $\beta_2 = 0$ and $\beta_2 = \pi/2$, respectively. Therefore $\mathcal{C}$ is nonzero only if $k \cos \vartheta > 2 \cos \alpha_2$ or, using optical coordinates

$$s > s_0 = \cos \alpha_2 / [2 \sin^2(\alpha/2)] \tag{2.32}$$

For low apertures $s_0$ becomes very large. The physical interpretation is that the envelope of the focus only transmits very low spatial frequency but the interference pattern transmits two additional, narrow frequency bands corresponding to its modulation period.

For the case of a cylindrically symmetric pupil function we have

$$\mathcal{C}_x = 16\pi \left( \mathcal{I}_0 + \mathcal{I}_1 \cos 2\varphi + \mathcal{I}_2 \cos 4\varphi \right) / k \tag{2.33a}$$

$$\mathcal{C}_y = 16\pi \left( \mathcal{I}_3 - \mathcal{I}_2 \cos 4\varphi \right) / k \tag{2.33b}$$

$$\mathcal{C}_z = 16\pi \left( \mathcal{I}_4 + \mathcal{I}_5 \cos 2\varphi \right) / k \tag{2.33c}$$

in complete analogy to equation (2.14) The integrals take a similar form as in equation (2.15) but the axial coordinate is inverted for the second pupil function and we have to include the phase factors from (2.30). Taking into account the integration range (2.31) we write

$$\mathcal{I}_i = \int_{\beta_2}^{\pi-\beta_2} \exp(i \cos(\vartheta_2)d_2 - i \cos(\vartheta_1)d_1) \mathcal{J}_i \, d\varphi'' P^* \left( \pi - \vartheta_1 \right) P \left( \vartheta_2 \right) \tag{2.34}$$

The integrands $\mathcal{J}_i$ are found by replacing $s_2$ with $-s_2$ in equations (2.25) due to the inversion of the axial coordinate by the matrix $\mathbf{M}$.

At arbitrary depths the foci of the two lenses would have to be re-aligned whenever the position of the focal plane in the sample changes. In practical 4Pi microscopy this problem can be avoided because at usual focusing depths the dependence of the focal shift is well approximated by a linear function for scan ranges of several tens of microns. The proportionality constant can be determined numerically and depends on the aperture angle and the refractive indices. For thin samples $\partial d/\partial \Delta$ is independent of the focus position and the alignment of the foci therefore doesn't change when moving the sample between the lenses. When focusing deeper $\partial d/\partial \Delta$ depends on $\Delta$ and therefore re-alignment can only be avoided near the central plane of the sample. It should also be noted that in all cases the position dependent phase shift of the maximum has to be compensated by varying the phase angle $\phi$ in order to maintain an approximately
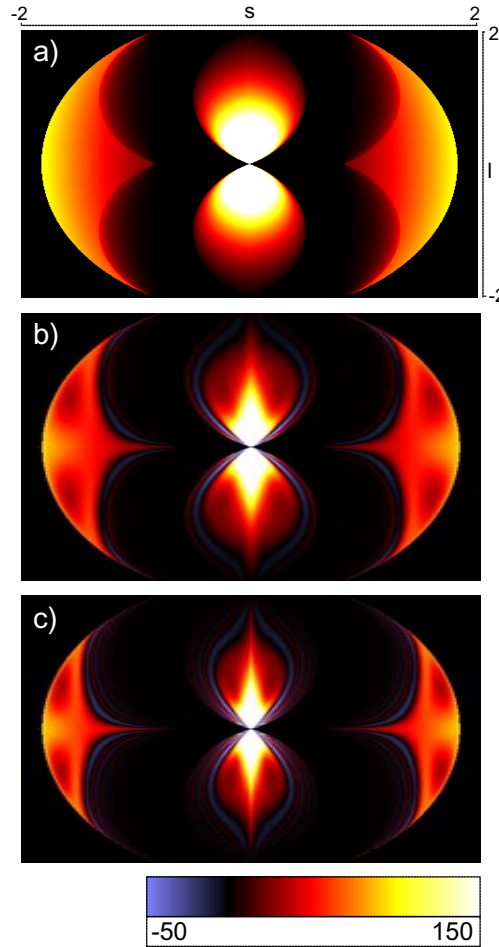
Figure 2.4:   *The excitation OTF of a 4Pi microscope (a) for an unaberrated system and (b,c) when focusing into 80% glycerol ($n_2 = 1.45$) with an oil ($n_1 = 1.52$) immersion lens The Gaussian focus of both lenses was assumed (b) $20\mu m$ and (c) $50\mu m$ deep in medium 2, corresponding to a PSF centered in $43.1\mu m$ and $106.4\mu m$ thick samples. The half aperture angle was $\alpha = 1.1$.*

space invariant PSF.[28] Figure 2.4 shows the OTF of a 4Pi system assuming that the focus is in the middle of the sample. Because the PSF is symmetric in this case the imaginary part of the OTF vanishes. We adjusted the thickness of the sample in order to obtain the same depth of the Gaussian focus as assumed for a single lens in figure 2.3. Because the origin was chosen in the maximum no oscillations along the axial coordinate occur for the aberrated cases. However the loss of transmitted frequencies due to spherical aberrations is obvious from the graph.

The formalism introduced here is not restricted to the calculation of excitation OTFs. Rather it allows to directly determine the Fourier transform of any product $f^*g$ of two field components, by using the appropriate strength factors. A possible example would be the energy flux given by the Pointing vector $\mathbf{h} \times \mathbf{e}$. In addition the Fourier transform of products $fg$ will be of interest, e.g. when describing confocal microscopes in reflection mode. The geometry is then changed and the necessary modifications to the formulae are described in appendix C.1.

## 2.4 Focal Heating by Linear Absorption

Biological specimen consist mainly of water which has a non-negligible absorption in the 700-1100nm wavelength range. Therefore, focal heating caused by linear absorption in the near infrared has been termed a limiting factor in optical trapping[29] and multiphoton microscopy.[30] Experimental studies[31] showed heating by slightly less than 3K for irradiation with 170mW at 1064nm through an oil immersion lens with a numerical aperture of NA=1.3. Theoretical estimates for the focal temperature rise were also published but they are based on simplified PSFs[32] or assumed an axially invariant Gaussian beam profile, which does not account for axial heat transport.[30] In order to obtain reliable results the true shape of the diffraction pattern should be used and the diffusion equation must be solved numerically. If $\Lambda$ and $c_{\mathrm{v}}$ are heat conductivity and volume heat capacity of a homogeneous medium it reads

$$\Big[c_{\mathrm{v}}\partial_t - \Lambda\nabla^2\Big]T(\mathbf{r}, t) = p(\mathbf{r}, t) \tag{2.35}$$

where $p$ is the absorbed power per unit volume and $T$ is the temperature. Let $h$ be the electric energy density normalized to 1 in its maximum and $\sigma$ the axial energy flux scaled accordingly. The absorbed power per volume is then given by

$$p(\mathbf{r}, t) = \gamma Ph(\mathbf{r}, t)/\sigma \tag{2.36}$$

with $P$ being the total incident power and $\gamma$ is the extinction coefficient of the medium. Assuming cylindrical symmetry and switching to optical coordinates and a dimensionless time scale $\tau = t/\tau_0$, $\tau_0 = [k^2(\mathrm{NA})^2\Lambda/c_v]$ equation (2.35) becomes

$$\Big[\partial_\tau - a^2\partial_u - \frac{1}{v}\partial_v v\partial_v\Big]T(v, u, \tau) = \xi h(v, u, \tau) \tag{2.37}$$

with $\xi = \gamma P/(\sigma \Lambda)$ defining the temperature scale and $a = 4\sin^2(\alpha/2)/\sin(\alpha)$ from the definition of the optical coordinates. For small aperture angles $\sigma$ can be approximated by the integral of $h$ over the focal plane denoted by $\sigma'$

$$\sigma' = 2\pi \int dv\, v\, h(v, u, \tau)\bigg|_{u=0} \tag{2.38}$$

but when the aperture increases one has to exclude the lateral component of the flux stemming from outer regions of the aperture. In scalar diffraction theory the field is a superposition of plane waves weighted with the pupil function and we have

$$\sigma = \sigma' \int d\Omega\, P(\theta)\cos\theta \Big/ \int d\Omega\, P(\theta) \tag{2.39}$$

In vectorial theory a more precise solution can be found integrating the pointing vector over a plane perpendicular to the optic axis. The ratio of $\sigma$ and $\sigma'$ was found to differ from the scalar approximation by less than 5%.

We assume that a constant irradiation starts at $\tau = 0$ and ends after a time span $\tau_1$. An upper bound for the temperature rise can be found by assuming an axially invariant beam with a Gaussian profile $h(v) = \exp(-\pi v^2/\sigma)$. In this case (2.37) can be integrated analytically. It is convenient to define $\bar{\tau} = \min(\tau, \tau_1)$; the solution is then

$$\Delta T(\tau) = \xi \left[\ln(1 + \tau) - \ln(1 + \tau - \bar{\tau})\right] \tag{2.40}$$

For $\tau < \tau_1$ the second addend disappears. The choice of $\sigma$ is somewhat arbitrary in this approach, which makes it inherently unreliable because the temperature rise in the focus scales with $\sigma^{-1}$. Here we adjusted the focal intensity to that predicted by scalar diffraction theory of an aplanatic system where $\sigma' \simeq 4\pi$ and (2.39) becomes

$$\sigma = 4\pi \cdot \tfrac{3}{5}(1 - \cos^{\frac{5}{2}}\alpha)/(1 - \cos^{\frac{3}{2}}\alpha) \tag{2.41}$$

Obtaining a more reliable prediction by numerically integrating (2.37) using the exact form of the diffraction pattern is difficult especially for long irradiation times, owing to the oscillatory nature of the PSF and the infinite integration range. However the differential equation simplifies in inverse space and because the diffraction pattern is bandwidth limited integrations will be over a finite volume. We therefore Fourier transform the heat equation

$$\left[\partial_\tau + l^2 + a^2 s^2\right]\hat{T}(l, s, \tau) = \xi C(l, s, \tau) \tag{2.42}$$

where $C(l, s, \tau)$ is the OTF of the lens, $C(l, s)$, during irradiation and zero otherwise. For irradiation between $\tau = 0$ and $\tau = \tau_1$ the formal solution to the problem is

$$\Delta \hat{T}(l, s, \tau) = \xi C(l, s) \int_0^{\bar{\tau}} d\tau' \exp\left(-[l^2 + a^2 s^2](\tau - \tau')\right) \qquad (2.43)$$

and carrying out the integral we obtain

$$\Delta \hat{T}(l, s, \tau) = \xi C(l, s)(l^2 + a^2 s^2)^{-1}$$
$$\times \left[\exp\left(-[l^2 + a^2 s^2](\tau - \bar{\tau})\right) - \exp\left(-[l^2 + a^2 s^2]\tau\right)\right] \quad (2.44)$$

For $\tau < \tau_1$ we have $\bar{\tau} = \tau$ and the first exponential becomes unity. The temperature can now be calculated by Fourier back-transforming the solution above.
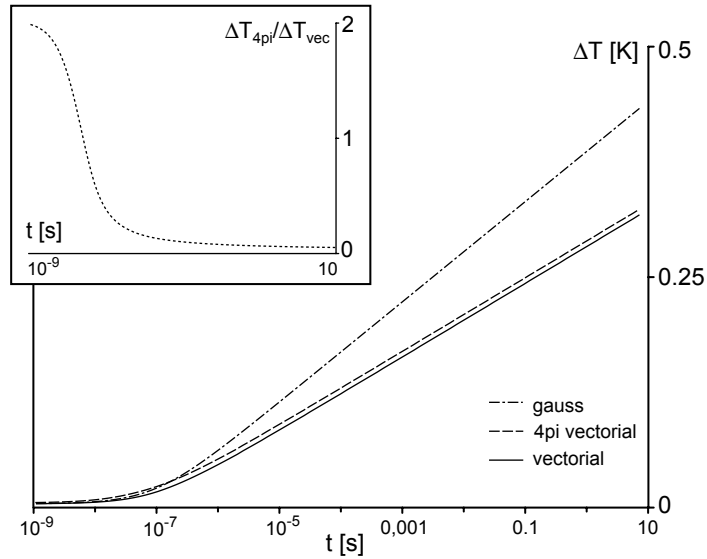


Figure 2.5: *Temperature rise due to water absorption in the center of the focal spot of a NA=1.2 water immersion lens during irradiation with 100mW at 850nm. The results for a single lens and a 4Pi setup are shown in comparison with the Gaussian model and inset compares the focal temperature in a 4Pi microscope to the values for a single lens.*

For long irradiation times $\Delta \hat{T}$ resembles a sharp peak around the origin, therefore an algorithm was implemented that successively contracts the integration area to ensure unchanging accuracy. All calculations were carried out for $NA = 1.2$ water immersion lenses with a relative precision of 1% and assuming $\Lambda = 0.6 \, \text{WK}^{-1}$,
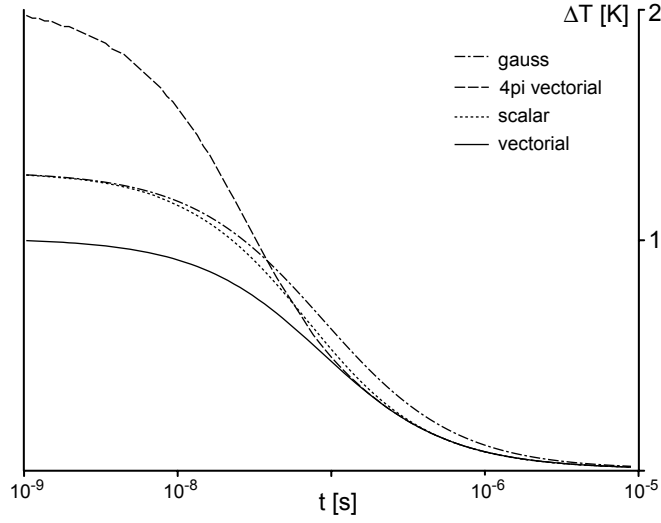
Figure 2.6: *Cooling of the focal spot after an irradiation with 500mW for 1ns resulting in transient heating of 1K for a single lens. The result for the Gaussian model and for scalar and vectorial diffraction theory are shown for a single lens. The cooling curve after irradiation with a 4Pi focus is also depicted.*

$c_v = 4.19\,\mathrm{JK^{-1}cm^{-3}}$, $\gamma = 0.013\,\mathrm{cm^{-1}}$. Figure 2.5 compares the temperature rise in the center of the focus of a single lens and for a constructive 4Pi diffraction pattern with equal total exposure. Due to the interference the electric energy density in the main maximum is twice higher for the 4Pi system and for short irradiation times the heating effect is thus doubled. However, the long term temperature rise mainly depends on heat transport over larger distances and thus on the envelope of the diffraction pattern and only a constant temperature offset remains due to recently deposited energy in the interference maximum. The results are also compared to the Gaussian model. As expected, disregarding axial

| NA | $\tau_0$ [ns] | $\Delta T$ [K] | $\Delta T'$[K] | $\Delta T/\Delta T' - 1$ [%] |
|----|------|-------|-------|------|
| 0.4 | 800 | 0.237 | 0.248 | 4.6 |
| 0.8 | 200 | 0.262 | 0.295 | 12.6 |
| 1.0 | 128 | 0.272 | 0.328 | 20.6 |
| 1.2 | 89 | 0.280 | 0.381 | 36.1 |
| 1.3 | 76 | 0.286 | 0.434 | 51.7 |

Table 2.1: *Temperature increase $\Delta T$ and logarithmic approximation $\Delta T'$ for different numerical apertures (NA) after irradiation of water with 100mW at 850nm for one second.*

| $\lambda$ [nm] | $\xi$ [K] | $\tau_0$ [ns] | $\Delta T$ [K] | | | |
|---:|---|---:|---|---|---|---|
| | | | 10s | 1s | 1ms | 1$\mu$s |
| 50 | 0.014 | 52 | 0.25 | 0.22 | 0.13 | 0.040 |
| 750 | 0.017 | 69 | 0.30 | 0.26 | 0.15 | 0.044 |
| 850 | 0.018 | 89 | 0.32 | 0.28 | 0.16 | 0.044 |
| 950 | 0.180 | 111 | 3.17 | 2.77 | 1.57 | 0.402 |
| 1050 | 0.152 | 136 | 2.65 | 2.31 | 1.30 | 0.315 |

Table 2.2: *Temperature increase for different wavelengths at NA=1.2 after irradiation of water with 100mW for different durations*

heat transport leads to an overestimation of the temperature rise by the logarithmic solution. This overestimation is expected to be larger for high numerical apertures, because heat dissipation along the optic axis becomes important due to strong axial focusing. This expectation is confirmed in table 2.1 where we compare our numerical results with the prediction of the Gaussian model. It is however important to keep in mind that the choice of $\sigma$ and thus the temperature scale is not rigorous in the latter case and in fact the ratio between both predictions stays almost constant over time. By 'switching off' axial heat transport in our numerical calculations it can be seen that the Gaussian model overestimates heating for short and long irradiation times owing to two different reasons. While inaccuracies in the lateral profile of the PSF result in an overestimation of the peak intensity and are thus responsible for the deviation at short times, the error for larger times is due to neglecting axial heat transport. This finding is also supported by the results shown in figure 2.6 where the cooling after short irradiation with an intensive light pulse is depicted. Again, the logarithmic approximation predicts higher values over the whole time scale. Numerical calculations based on the scalar OTF initially deliver the same values because the same value for $\sigma$ is assumed but as heat dissipation becomes more important the scalar solution approaches the vectorial model while the Gaussian model remains inaccurate due to its inherent simplifications. As expected, the pulse heats the center of a 4Pi PSF twice more but the temperature soon approaches that of a single lens because the initial pattern is smeared out. Finally table 2.2 shows focal heating owing to water absorption for different wavelengths and irradiation times. It is expected to remain less then 3K for all cases shown. The numerical results can be used to estimate heating for arbitrary irradiation times, media and wavelengths by calculating $\tau_0$ and $\xi$ and rescaling the graphs in figure 2.5. It should be mentioned that all calculations assumed samples with infinite boundaries. In reality it is in con-

tact with the microscope and the coverslip both of which can act as a heat sink. Therefore long-term heating is slightly overestimated by the logarithmic increase and our predictions are upper bounds. Heating by two-photon absorption can be calculated using a three-dimensional Gaussian and solving the heat equation analytically. For micromolar absorber concentrations sub-millikelvin effects are predicted for typical conditions.

# Chapter 3

# Patterned Correlation Spectroscopy

Fluorescence correlation spectroscopy (FCS) is a long established tool for the investigation of dynamic processes in solutions using the fluorescence signal from a, usually small, detection volume.[1] Fluid motion and the reactions among its constituents are theoretically modelled and the model parameters are determined by fitting the time correlation of the signal.

If the form of the detection volume is not carefully controlled the precision of such measurements is compromised. Often fluorescent particles in the fluid undergo photophysical reactions, such as photobleaching, which take place on similar time scales as diffusion or drift from the detection volume. In such cases the effects of particle motion on the correlation curve are difficult to separate from those due to reactions.

While models for anisotropic diffusion or particle drift can be included in standard FCS, it is inherently insensitive to the direction of the particle movement. The axes belonging to different diffusion constants parallel to the focal plane are impossible to distinguish and for diffraction limited spots even axial diffusion is difficult to separate. Extensive a priori knowledge is thus a prerequisite when trying to extract this information by correlating the signal from an unstructured focal spot.[33,34]

Here this problem is addressed by superimposing a pattern on the focal spot and thus designating a direction and introducing a precise length scale to the experiment. A modulation of the detection volume with a periodic pattern was proposed as early as 1975 by Asai and Ando[35]. They suggested to create a

standing wave of excitation light using a mirror at the end of the sample chamber. This concept was extended and experimentally implemented by Lenne and coworkers[36]. By focusing the laser beam onto a mirror with an objective lens and using confocal detection they created a diffraction limited, patterned detection volume but such experiments are limited to the immediate proximity of the mirror. The signal is enhanced because the mirror reflects fluorescence photons into the detector. However, this also distorts the detection volume which complicates precise data analysis. Bardeen and Coworkers used standing waves in two-photon patterned photobleaching experiments[37] in order to measure intracellular diffusion constants. Because they employed two opposing lenses instead of a mirror to create the standing wave, diffusion could be measured at arbitrary axial positions in the sample.

As an alternative to the axial pattern, two coherent laser beams can be crossed in the focal region producing a lateral interference pattern. Several approaches exist to combine such a setup with correlation measurements using static[38] or travelling[39] interference fringes. In fact, due to the large focal spot used in these systems a single frequency component of the particle distribution is measured. As before, the data can be used to extract model parameters, however the spacing of the fringes can also be varied by tilting the beams relative to each other. The intermediate scattering function which describes the dynamics of a complex fluid is then directly measured. This technique has recently been introduced and is called Fourier imaging correlation spectroscopy[40] (FICS). Because the large detection volume is intrinsic to this class of measurements, spatial variations of fluid properties are difficult to determine and anisotropic systems require a way to control both the pattern's spacing and orientation.

Here, a vectorial theory for combining FCS with spatially modulated PSFs in high resolution microscopy is developed in full generality. The model used for the fluid allows for anisotropic diffusion and drift of the particles and a method to determine all related parameters is proposed. Because it is based on comparing correlation curves recorded with patterned and unpatterned detection volumes, effects which do not depend on the particles's motion cancel out and no longer compromise data analysis.

## 3.1 Theory of Correlation Measurements

All fluorescence correlation techniques record the time correlation of two detection channels with the autocorrelation of a single channel just being a special case. Usually the data is normalized by the average signals and the constant offset is subtracted

$$G(\tau) = [\langle F_1 \rangle \langle F_2 \rangle]^{-1} \langle F_1(t) F_2(t+\tau) \rangle - 1 \qquad (3.1)$$

The time average $\langle \rangle$ is assumed to be taken over a measurement period much longer than the time scale $\tau$ we are interested in. In this form, the signal $G(\tau)$ effectively measures the correlation of the signal fluctuations $\langle \delta F \rangle$

$$G(\tau) = [\langle F_1 \rangle \langle F_2 \rangle]^{-1} \langle \delta F_1(t) \delta F_2(t+\tau) \rangle \qquad (3.2)$$

Now let $N$ types of particles be present in the sample. We denote the rate of fluorescence photons detected in channel $n$ from a particle of type $j$, which is located at position $\mathbf{r}$ at a given time $t$ by $Q_{jn} h_n(\mathbf{r}, t)$ where the particle brightness $Q_{jn}$ is a constant for each particle and $h_n$ is the spatial and temporal form of a channel's detection volume, normalized to unity in its maximum. In general, $Q$ will contain information about excitation cross section, quantum efficiency and spectral detection probability for the particle type, while $h$ is the normalized effective point spread function (PSF) of the optical setup. If the concentration of the $j$th particle type is denoted by $C_j(\mathbf{r}, t)$, the signal in channel $n$ is given by

$$F_n(t) = \sum_{j=1}^{N} \int d^3 r Q_{nj} h_n(\mathbf{r}, t) C_j(\mathbf{r}, t) \qquad (3.3)$$

We will restrict our analysis to cases where particle concentration, spectroscopical properties, and the point spread function are uncorrelated in time, that is $\langle QhC \rangle = \langle Q \rangle \langle h \rangle \langle C \rangle$. If we define the time averaged volume integrals of our PSFs

$$V_n = \int d^3 r \langle h_n(\mathbf{r}) \rangle \qquad (3.4)$$

and assume that the time average of the concentrations is spatially invariant the average detector signal is given by

$$\langle F_n \rangle = V_n \sum_{j=1}^{N} \langle C_j \rangle \langle Q_{nj} \rangle \qquad (3.5)$$

and the correlation curve takes the form

$$G(\tau) = [\langle F_1 \rangle \langle F_2 \rangle]^{-1} \int d^3 r d^3 r' \sum_{j,k=1}^{N} \langle Q_{1k} Q_{2j} \rangle \, \phi_{jk} \left( \mathbf{r} - \mathbf{r}', \tau \right)$$
$$\times \langle h_1 \left( \mathbf{r}', t \right) h_2 \left( \mathbf{r}, t + \tau \right) \rangle \quad (3.6)$$

where we assumed translational invariance and $\phi$ is the concentration correlation function given by

$$\phi_{jk} \left( \mathbf{r} - \mathbf{r}', \tau \right) = \langle \delta C_j \left( \mathbf{r} - \mathbf{r}', t + \tau \right) \delta C_k \left( 0, t \right) \rangle \quad (3.7)$$

The meaning of the concentration correlation function is put into context with the theory of complex fluids in appendix A.1. In a thin, homogeneous solution it is proportional to the probability that a particle of type $k$ which is located at $\mathbf{r}'$ moves to $\mathbf{r}$ and reacts to a particle of type $j$ during the time interval $\tau$. The expression for $G$ can be simplified by rewriting it as a single frequency integral. We use the identity

$$\mathcal{F}[(\phi_{jk} \otimes h_{1k}) \cdot h_{2j}] = (2\pi)^{-3} [(\hat{\phi}_{jk} \cdot \hat{h}_{1k}) \otimes \hat{h}_{2j}] \quad (3.8)$$

which can be verified by applying the convolution theorem twice. Its left hand side evaluated at the origin is equivalent to equation (3.6). Writing the convolution on the right hand side as an integral we obtain

$$G(\tau) = [\langle F_1 \rangle \langle F_2 \rangle]^{-1} (2\pi)^{-3} \int d^3 k \sum_{j,k=1}^{N} \langle Q_{1k} Q_{2j} \rangle \, \hat{\phi}_{jk} \left( \mathbf{k}, \tau \right)$$
$$\times \left\langle \hat{h}_1 \left( \mathbf{k}, t \right) \hat{h}_2 \left( -\mathbf{k}, t + \tau \right) \right\rangle \quad (3.9)$$

Because only a single integration is involved, this expression is more suitable for our theoretical analysis. For the same reason and because the OTF, $\hat{h}$, is usually bandwidth limited, it should be equally useful for numerical calculations.

## 3.2   The Fluid Model

We consider a solution consisting of a solvent and the particles under consideration. Let us assume that the interaction among the particles can be described by linear rate equations with the reaction rates given by the matrix $\mathbf{T}$. For electronic transitions in molecules this description is accurate and for reactions among

different particle types it is justified if the concentration fluctuations around equilibrium are small. The rates are assumed to be constant across the detection volume. Because modelling becomes exceedingly difficult without this assumption it is often used as an approximation, even when analyzing intensity dependent reactions like triplet state transitions in dye molecules.[41] In addition we allow for anisotropic diffusion described by a tensor $\mathbf{D}$ and a constant flow given by the vector $\mathbf{v}$. The tensor $\mathbf{D}$ is symmetric and its eigenvalues and mutually orthogonal eigenvectors correspond to the principal directions of diffusion and the related diffusion constants. Like the reaction rates, both flow and diffusion are assumed to be uniform within the detection volume. The differential equation describing the particle concentrations is then

$$\partial_t C_j = -\mathbf{v}^t \boldsymbol{\nabla} C_j + \sum_{m=1}^{N} T_{jm} C_m + \boldsymbol{\nabla}^t \mathbf{D} \boldsymbol{\nabla} C_j \tag{3.10}$$

Using (A.5) and (A.8) we obtain for the Fourier transform of the concentration correlation function with respect to $\mathbf{r}$

$$\partial_\tau \hat{\phi}_{jk} = i\mathbf{v}^t \mathbf{k} \hat{\phi}_{jk} + \sum_{m=1}^{N} T_{jm} \hat{\phi}_{mk} - \mathbf{k}^t \mathbf{D} \mathbf{k} \hat{\phi}_{jk} \tag{3.11}$$

In case the diffusion constants are equal for all species this differential equation is solved by

$$\hat{\phi}_{jk}(\mathbf{k}) = \hat{\alpha}(\mathbf{k}, \tau) S_{jk}(\tau) \tag{3.12}$$

with the $S_{jk}$ being solutions to the homogeneous linear differential equation

$$\partial_\tau S_{jk}(\tau) = \sum_{m=1}^{N} T_{jm} S_{mk}(\tau) \tag{3.13}$$

and

$$\hat{\alpha}(\mathbf{k}, \tau) = \exp\left(-\tau \mathbf{k}^t \mathbf{D} \mathbf{k} + i\tau \mathbf{v}^t \mathbf{k}\right) \tag{3.14}$$

In a homogeneous solution the probability of finding a molecule in an infinitesimal volume element at time $t$ is spatially invariant and therefore the number of molecules within any given volume at a random point in time is spatially uncorrelated and obeys the Poisson statistics. Therefore we can write

$$\phi_{jk}(\mathbf{r}, 0) = \delta_{jk} \delta(\mathbf{r}) \langle \delta C_j^2 \rangle = \delta_{jk} \delta(\mathbf{r}) \langle C_j \rangle \tag{3.15}$$

and after Fourier transformation we obtain the initial condition for equation (3.13)

$$S_{jk}(0) = \hat{\phi}_{jk}(\mathbf{k}, 0) = \langle C_j \rangle \delta_{jk} \tag{3.16}$$

Introducing the average particle brightness

$$\mathcal{Q}_l = \sum_{j=1}^{N} \langle Q_{lj} \rangle \langle C_j \rangle \tag{3.17}$$

the correlation function is given by

$$G(\tau) = \sum_{j,k=1}^{N} \langle Q_{1k} Q_{2j} \rangle \, S_{jk}(\tau) g(\tau) \Big/ \mathcal{Q}_1 \mathcal{Q}_2 \tag{3.18}$$

where the dimensionless function

$$g(\tau) = \int d^3 k \left\langle \hat{h}_1(\mathbf{k},t) \hat{h}_2(-\mathbf{k},t+\tau) \right\rangle \hat{\alpha}(\mathbf{k},\tau) / V_1 V_2 (2\pi)^3 \tag{3.19}$$

describes the effect of the detection volumes' shape on the correlation signal.
When the particles under consideration are not point-like luminescent dipoles but extended objects such as diffusing fluorescent beads which consist of many transition dipoles distributed over their volume or surface, the effective PSF of the system is changed. We introduce an object function, $\rho_j(\mathbf{r})$, which can be interpreted as a "transition dipole density". As a convention we will normalize its volume integral to unity, while the particle brightness is contained in the factors $Q_{lj}$. If the particles can be assumed to be approximately monodisperse and rotationally symmetric, the effective PSF is simply convolved with this object function. Due to the convolution theorem this is equivalent to a multiplication of the OTF with the Fourier transform $\hat{\rho}$. Therefore the integrands of (3.19) and (3.9) have to be multiplied by a factor $\hat{\rho}_j(\mathbf{k})\hat{\rho}_k(\mathbf{k})$ accounting for particle size effects.

## 3.3 Analytical Approximation

Because the theoretical description of FCS is used for the estimation of diffusion times and reaction parameters, a fast way to calculate the function $g(\tau)$ is essential for the successful application of nonlinear fitting methods. An analytical expression for the correlation function can be found when the PSFs are approximated by a three dimensional Gaussian

$$h(\mathbf{r}) = \exp(-2\mathbf{r}^t \mathbf{A}^{-1} \mathbf{r}) \tag{3.20}$$

The matrix A is symmetric, so there are three principal axes described by a system of orthonormal eigenvectors, $\mathbf{e}_j$ with the $1/e^2$ radii of the Gaussian given

by the corresponding positive eigenvalues, $\nu_j$. We use the identity (B.1) to Fourier transform the PSF and obtain

$$\hat{h}(\mathbf{k}) = V \exp(-\mathbf{k}^t \mathbf{A} \mathbf{k}/8) \tag{3.21}$$

where $V$ is the volume integral of the PSF and given by

$$V = \left(\det\left(\mathbf{A}\right) \pi^3/8\right)^{1/2} \tag{3.22}$$

We assume that the PSFs have the same form for both detectors but allow them to be offset by a distance $\mathbf{d}$, a setup frequently encountered in flow measurements

$$\hat{h}_1\left(\mathbf{k}\right) = \hat{h}\left(\mathbf{k}\right) \tag{3.23}$$

$$\hat{h}_2\left(\mathbf{k}\right) = \hat{h}\left(\mathbf{k}\right) \exp\left(-i\mathbf{k}\mathbf{d}\right) \tag{3.24}$$

In addition we approximate a finite particle size by a Gaussian object function

$$\hat{\rho}(\mathbf{k}) = \exp(-k^2 R^2/8) \tag{3.25}$$

The volume factors in (3.19) and (3.21) cancel out and the integral takes the form

$$g(\tau) = \int d^3k \exp\left(-\mathbf{k}^t \mathbf{A}(\tau)\mathbf{k}/4 - i\mathbf{k}^t \left(\tau\mathbf{v} - \mathbf{d}\right)\right)/(2\pi)^3 \tag{3.26}$$

where we defined the real, symmetric matrix

$$\mathbf{A}(\tau) = \mathbf{A} + R^2\,\mathbf{I} + 4\mathbf{D}\tau \tag{3.27}$$

with $\mathbf{I}$ being the identity matrix. Using the formula (B.1) once more, we find the result

$$g(\tau) = \exp\left(-\left[\tau\mathbf{v} - \mathbf{d}\right]^t \mathbf{A}(\tau)^{-1} \left[\tau\mathbf{v} - \mathbf{d}\right]\right)\Big/\sqrt{\pi^3 \det\left(\mathbf{A}(\tau)\right)} \tag{3.28}$$

The root in the denominator describes the influence of diffusion while the exponential term is due to the particle drift. When the offset $\mathbf{d}$ between two cross correlated detection volumes is oriented along its direction a local maximum is generated at $\tau = d/v$ allowing for the determination of the particle speed.

If diffusion is isotropic or the diffusion tensor and the matrix $A$ can be simultaneously diagonalized owing to an appropriate choice of the PSF's orientation, the result can be simplified. Let $D_j$ denote the eigenvalue of the diffusion tensor corresponding to the common eigenvector $\mathbf{e}_j$. We can then define the diffusion times

$$\tau_j = (R^2 + \nu_j^2)/4D_j \tag{3.29}$$

which can be interpreted as the time, a particle needs to cross the detection volume in the direction of the eigenvector. It is conventional to define an effective sample volume

$$V = \left[\pi^3(\nu_1^2 + R^2)(\nu_2^2 + R^2)(\nu_3^2 + R^2)\right]^{\frac{1}{2}} \tag{3.30}$$

obtaining the well known result

$$g_c(\tau) = V^{-1}[(1 - \tau/\tau_1)(1 - \tau/\tau_2)(1 - \tau/\tau_3)]^{-1/2}$$
$$\times \exp\left(-\sum_j [v_j\tau - d_\nu]^2/\nu_j^2 a_j(\tau)\right) \tag{3.31}$$

where we abbreviated

$$a_j(\tau) = (R^2 + \nu_j^2 + 4D_j\tau)/\nu_j^2 \tag{3.32}$$

For each fluorescing species we define the average number of particles contributing to the measurement

$$\langle N_i \rangle = V \langle C_i \rangle \tag{3.33}$$

If only one species fluoresces we obtain the famous relationship

$$G_c(0) = 1/\langle N_i \rangle \tag{3.34}$$

which states that the amplitude of the correlation function is inversely proportional to the number of fluorescent particles in the sample volume. Equation (3.31) proved useful for the rather simple case of isotropic diffusion and a cigar shaped PSF with rotational symmetry around the optic axis but cannot be used to extract information about the flow direction or the parameters of anisotropic diffusion.

## 3.4  Patterned Excitation

If we superimpose the PSF with a pattern and its period is well known, a precise time scale and a designated direction is created. The resulting correlation curve should therefore contain additional information about the movement of particles along the pattern which cannot be extracted from conventional experiments. Let the orientation and period of the pattern be given by the vector $\boldsymbol{\kappa}$ and $4\pi/\kappa$ respectively. We assume an optional, time dependent phase shift which is allowed to differ for the two detection channels. The modulation pattern can then be

written as a Fourier sum

$$h_n(\mathbf{r}, \boldsymbol{\kappa}, t) = h_e(\mathbf{r}) \sum_l B_l \exp(2il[\boldsymbol{\kappa}^t \mathbf{r} - \varphi_n(t)]) \tag{3.35}$$

$h_e$ is the envelope of the pattern and we have $B_{-l} = B_l^*$ because the intensity pattern is a real function. Using the convolution theorem, the Fourier transform of the new PSF is found

$$\hat{h}_n(\mathbf{k}, \boldsymbol{\kappa}, t) = \sum_l B_l \exp\left(2il\varphi_n(t)\right) \hat{h}_e(\mathbf{k} - 2l\boldsymbol{\kappa}) \tag{3.36}$$

Substituting it into equation (3.19) we obtain a double sum for the geometrical part of the correlation function

$$g(\tau) = V_e^2/V^2 \sum_{l,m} B_l B_m J_{lm}(\boldsymbol{\kappa}, \tau) \left\langle \exp\left(2il\varphi_1(t) + 2im\varphi_2(t + \tau)\right) \right\rangle \tag{3.37}$$

with the frequency integral given by

$$J_{lm}(\boldsymbol{\kappa}, \tau) = \int d^3k \; \hat{\alpha}(\mathbf{k}, \tau) \, \hat{\rho}(\mathbf{k})^2 \, \hat{h}_e(2l\boldsymbol{\kappa} + \mathbf{k}) \, \hat{h}_e(2m\boldsymbol{\kappa} - \mathbf{k}) \tag{3.38}$$

In order to simplify this result we use the Gaussian approximation for the envelope and the particle shape. Substituting equation (3.14) and using the definition (3.27) we obtain

$$J_{lm}(\boldsymbol{\kappa}, \tau) = \int d^3k \exp(-\mathbf{k}^t \mathbf{A}(\tau) \mathbf{k}/4 - i\tau \mathbf{k}^t \mathbf{v})/(2\pi)^3$$
$$\times \exp\left((l - m)\mathbf{k}^t \mathbf{A}\boldsymbol{\kappa}/2\right) \exp\left(-(l^2 + m^2)\boldsymbol{\kappa}^t \mathbf{A}\boldsymbol{\kappa}/2\right) \tag{3.39}$$

We define the matrix

$$\mathbf{E}(\tau) = \mathbf{A}\mathbf{A}(\tau)^{-1} \tag{3.40}$$

and use (B.1) once more to carry out the integral. The contribution of the envelope $g_e$ is given by (3.28) with $\mathbf{d} = 0$ and can be factored out. The solution then reads

$$J_{lm}(\boldsymbol{\kappa}, \tau) = g_e(\tau) \exp\left(-(l + m)^2 \boldsymbol{\kappa}^t \mathbf{E}(\tau)\mathbf{A}\boldsymbol{\kappa}/4\right)$$
$$\times \exp\left(-(l^2 + m^2)\boldsymbol{\kappa}^t \mathbf{E}(\tau)(4\mathbf{D}\tau + \mathbf{I}R^2)\boldsymbol{\kappa}/2\right)$$
$$\times \exp\left(i(l - m)\tau \boldsymbol{\kappa}^t \mathbf{E}(\tau)\mathbf{v}\right) \tag{3.41}$$

where we used the identity

$$\mathbf{E}(\tau)\mathbf{A} + \mathbf{E}(\tau)(4\mathbf{D}\tau + \mathbf{I}R^2) = \mathbf{A} \tag{3.42}$$

to reorder the contributions. Let us now assume that the phase varies at a constant rate, that is $\varphi_n(t) = \omega t + \phi_n$. In this case the time average in equation (3.37) is nonzero only for $l = -m$ and we are left with a single sum. The volume integral of the PSF is the value of the OTF at the origin. If we assume that at least one period of the pattern is contained in the envelope of the PSF we have

$$\exp(-\boldsymbol{\kappa}^t \mathbf{A} \boldsymbol{\kappa}) \ll 1 \tag{3.43}$$

and therefore from (3.36)

$$V = \left\langle \hat{h}(0, t) \right\rangle \simeq V_e B_0 \tag{3.44}$$

At small $\tau$, where the correlation function has still a significant amplitude, equation (3.43) generalizes to

$$\exp(-\boldsymbol{\kappa}^t \mathbf{E}(\tau) \mathbf{A} \boldsymbol{\kappa}) \ll 1 \tag{3.45}$$

Therefore the factor in the first line of equation (3.41) is small for all $l \neq -m$ and these contributions can be neglected even when the phase is kept constant or exhibits a more complex time dependence as assumed above. If the correlation function is recorded for both the patterned PSF and the envelope the ratio of the two curves is independent of the spectroscopical properties of the particles. Using equations (3.18) and (3.44) we obtain

$$G(\tau)/G_e(\tau) = \sum_l \mathcal{P}_l(\tau) |B_l|^2 / B_0^2$$
$$\times \exp\left(-4l^2 \tau \boldsymbol{\kappa}^t \mathbf{E}(\tau) \mathbf{D} \boldsymbol{\kappa}\right) \exp\left(2il\left[(\boldsymbol{\kappa}^t \mathbf{E}(\tau) \mathbf{v} - \omega)\tau + \Delta\phi\right]\right) \tag{3.46}$$

Where $\Delta\phi = \phi_1 - \phi_2$ is the relative phase offset of the two channels and the newly introduced function

$$\mathcal{P}_l(\tau) = \exp\left(-R^2 l^2 \boldsymbol{\kappa}^t \mathbf{E}(\tau) \boldsymbol{\kappa}\right) \tag{3.47}$$

describes the damping of the pattern effect due to the finite size of particles. As it could be expected this function mainly depends on the size ratio of particles and pattern and the contributions from higher harmonics are more effectively damped. For very large particles the pattern is smeared out and the original correlation curve is reproduced. By subtracting the constant offset we introduce the directional correlation function

$$\gamma(\tau, \omega, \boldsymbol{\kappa}) = G(\tau)/G_e(\tau) - 1 \tag{3.48}$$

and using the symmetry of the real factors in (3.41) with respect to $l$ we restrict the summation to positive $l$ and obtain

$$
\gamma(\tau, \omega, \boldsymbol{\kappa}) = 2 \sum_{l>0} \mathcal{P}_l(\tau) |B_l|^2 / B_0^2
$$
$$
\times \exp\left(-4l^2 \tau \boldsymbol{\kappa}^t \mathbf{E}(\tau) \mathbf{D}\boldsymbol{\kappa}\right) \cos\left(2l\left[(\boldsymbol{\kappa}^t \mathbf{E}(\tau)\mathbf{v} - \omega)\tau + \Delta\phi\right]\right) \quad (3.49)
$$

Importantly all dependence on reactions taking place in the sample is removed from this observable Moreover the amplitude of $\gamma$ is independent of relative quantum yields and detection probabilities. In principle this result can be used to measure all parameters of particle movement. If the vector $\boldsymbol{\kappa}$ can be chosen at will, equation (3.49) allows for determination of the tensor $\mathbf{D}$ and the flow vector $\mathbf{v}$ by a series of experiments with various pattern orientations. In order to determine both magnitude and sign of the flow vector's components one either has to record curves with distinct values for $\omega$ or introduce a phase difference $\Delta\phi$ between the detection channels.

## 3.5 Frequency Filtering

In order to simplify data analysis and reduce the number of measurements needed the method can be combined with lock-in detection by varying the phase of the modulation patterns at frequencies faster than the measured correlations and detecting only the corresponding frequency component of the signal. Hardware based frequency selection using the lock-in method can use frequencies faster than the smallest time bin accessible by the counting hardware and it is compatible with the logarithmic detection scheme of hardware correlators.[42] Let us therefore assume that our setup can modulate the detection probability of both detection channels at a common lock-in frequency $\omega_L$ but with independent phase offsets $\phi_n$. The time modulation function can then be written as a Fourier sum

$$
f_n(t) = \sum_l L_l \exp(il[\omega_L t + \phi_n]) \quad (3.50)
$$

where the offset $\phi_n$ is usually unknown but its time dependence and the phase difference of both channels $\Delta\phi = \phi_1 - \phi_2$ can be adjusted. In practice the hardware actually averages the signal over time bins of width $\Delta t$ which we assume to be much longer than the detector response function. If $h'_n$ denotes the PSFs in the absence of lock-in detection the new effective PSF is well approximated by

$$
h_n(\mathbf{r}, t) = \int_0^{\Delta t} ds \, h'_n(\mathbf{r}, t+s) f_n(t+s)/\Delta t \quad (3.51)
$$

We vary the pattern's phase at a constant rate $\varphi_n(t) = \omega t$ and choose the modulation frequency $\omega = 2\pi/\Delta t$. Now one hardware time-bin corresponds to a full oscillation of the PSFs. Choosing $\omega_L = 2\omega$ as lock-in frequency we obtain the effective PSF

$$h_n(\mathbf{r}, \boldsymbol{\kappa}, t) = h_e(\mathbf{r}) \sum_l B_l L_l \exp\big(il[2\boldsymbol{\kappa}^t\mathbf{r} + \phi_n]\big) \tag{3.52}$$

Because the time-average of the modulated signal depends on the form of $f$ and can approach zero, we choose to normalize our correlation curve with the average of the unmodulated signal which will be detected in a separate channel. The offset subtracted in the definition of the directional correlation function has to be adjusted accordingly and we define

$$\gamma(\tau, \Delta\phi, \boldsymbol{\kappa}) = G(\tau)/G_e(\tau) - |L_0|^2 \tag{3.53}$$

and in analogy to equation (3.49)

$$\gamma(\tau, \Delta\phi, \boldsymbol{\kappa}) = 2 \sum_{l>0} \mathcal{P}_l(\tau)|L_l B_l|^2/B_0^2$$
$$\times \exp\left(-4l^2\tau\boldsymbol{\kappa}^t\mathbf{E}(\tau)\mathbf{D}\boldsymbol{\kappa}\right) \cos\left(l\big[2\tau\boldsymbol{\kappa}^t\mathbf{E}(\tau)\mathbf{v} + \Delta\phi\big]\right) \tag{3.54}$$

It is interesting to note that the FICS technique mentioned in the introduction relies on a similar measurement principle. In short it can be described by considering the limiting case of infinitely large focal spots in the theory above. A more detailed comparison is given in appendix A.2.

Let us now assume that the $L_l$ and $B_l$ drop off sufficiently fast so we can neglect all higher harmonics. In order to maximize the information that can be extracted from our data one can measure correlation curves for two different phase offsets $\Delta\phi$ and the unmodulated curve simultaneously. This is achieved by splitting the detector signal into three channels and recording the unmodulated signal $F_e$ in one of them. In two additional channels, the two modulated signals, $F_1$ and $F_2$ are recorded but the modulation's phase is shifted by $\pi/2$ for $F_2$. Because the time average of the PSF is proportional to its envelope the function $G_e$ is just the autocorrelation of $F_e$. In addition we record the autocorrelation of $F_1$, $G_a$, and the cross-correlation of $F_1$ and $F_2$, $G_x$. The corresponding directional correlation functions evaluate to

$$\gamma_a(\boldsymbol{\kappa}, \tau) = G_a/G_c = \gamma_s(\boldsymbol{\kappa}, \tau) \cos\left(2\tau\boldsymbol{\kappa}^t\mathbf{E}(\tau)\mathbf{v}\right) \tag{3.55}$$

$$\gamma_x(\boldsymbol{\kappa}, \tau) = G_x/G_c = \gamma_s(\boldsymbol{\kappa}, \tau) \sin\left(2\tau\boldsymbol{\kappa}^t\mathbf{E}(\tau)\mathbf{v}\right) \tag{3.56}$$

where we introduced the function

$$\gamma_s(\boldsymbol{\kappa}, \tau) = \sqrt{G_a^2 + G_x^2}/G_c =$$
$$2\left|L_1 B_1\right|^2 / B_0^2 \, \mathcal{P}_1(\tau) \exp\left(-4\tau \boldsymbol{\kappa}^t \mathbf{E}(\tau) \mathbf{D} \boldsymbol{\kappa}\right) \quad (3.57)$$

which is independent of the particle flow. This elaborate detection scheme was chosen because the diffusion constant and the magnitude of the flow along the pattern can be more reliably extracted from $\gamma_a$, while the sign of the flow vector's components is identified by $\gamma_x$. In fact, if both curves are simultaneously analyzed information about flow and diffusion can be separated because $\gamma_s$ is independent of flow.

When the principle directions of diffusion are aligned with the PSF, the result for a measurement along the $jth$ axis of the PSF simplifies to

$$\gamma_a(\tau, \kappa) = \gamma_s(\tau) \cos(2\tau \kappa v_j / a_j(\tau)) \tag{3.58}$$

$$\gamma_x(\tau, \kappa) = \gamma_s(\tau) \sin(2\tau \kappa v_j / a_j(\tau)) \tag{3.59}$$

and remembering the definition of the damping function, the common dependence on diffusion is given by

$$\gamma_s(\tau, \kappa) = 4B_1^2/(\pi^2 B_0^2) \exp(-R^2 \kappa^2 / a_j(\tau)) \exp(-4\tau \kappa^2 D_j / a_j(\tau)) \tag{3.60}$$

The signal is now formed exclusively by diffusion and flow along the pattern.

## 3.6 Experimental Realization

The goal is to fit correlation curves recorded at different points of the sample using the model developed above and extract flow and diffusion parameters, thus effectively imaging particle flow and diffusion throughout the sample. In order to achieve reasonable spatial resolution we will ideally need diffraction limited focal spots with a superimposed pattern which cannot be produced by intersecting Gaussian beams. However such spots with the pattern along the optic axis are already used in 4pi confocal microscopes where the modulation is due to the interference of two counterprobagating laser beams and can be shifted within its envelope by varying their relative phase.[43] Figure 3.1 shows the detection probability in the focal region of a 4pi microscope using one-photon excitation. The excitation field was calculated based on the theory of Richards and Wolf[23].

For determination of the detection probability an Airy-disk sized pinhole was assumed. In general the n-photon 4pi PSF is well approximated by

$$h(\mathbf{r}, \boldsymbol{\kappa}, t) = h_e(\mathbf{r}) \big[\cos(\omega t - \boldsymbol{\kappa}^t \mathbf{r})\big]^{2n} \tag{3.61}$$

where $h_e$ denotes the envelope of the pattern which is equivalent to a confocal PSF. The vector $\boldsymbol{\kappa}$ is oriented along the z-axis and slightly larger than the wave vector of the light, owing to the high aperture of the lens. Using the identity $\cos x = (e^{ix} + e^{-ix})/2$ we find the Fourier coefficients

$$B_l = 4^{-n} \binom{2n}{n+l} \tag{3.62}$$

where of course $l \leq n$. Let us further assume that the correlation hardware can switch between adding and subtracting the detected photons at the lock-in frequency. The first Fourier coefficients of such a rectangular function are
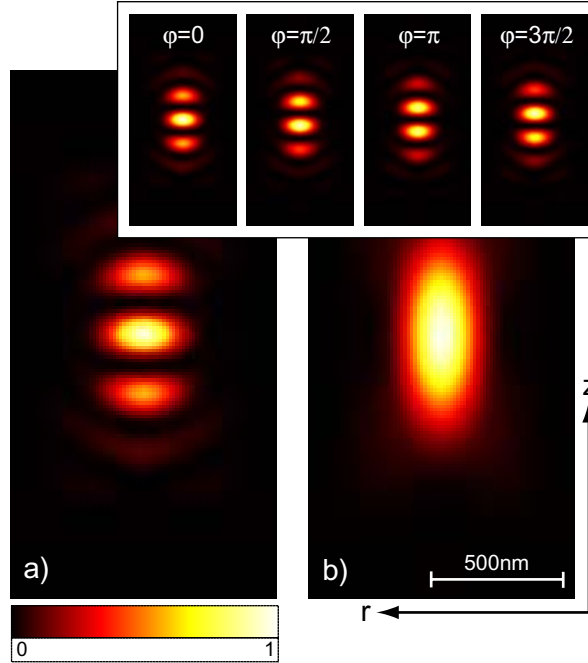


Figure 3.1:   *(a) The PSF of a one-photon type A 4pi confocal microscope calculated for 488nm excitation light, a numerical aperture of 1.2 in water and an Airy-disk sized pinhole. The inlay shows the movement of the pattern when varying the phase difference of the beams. (b) The time average of a moving pattern which is equivalent to a confocal PSF.*
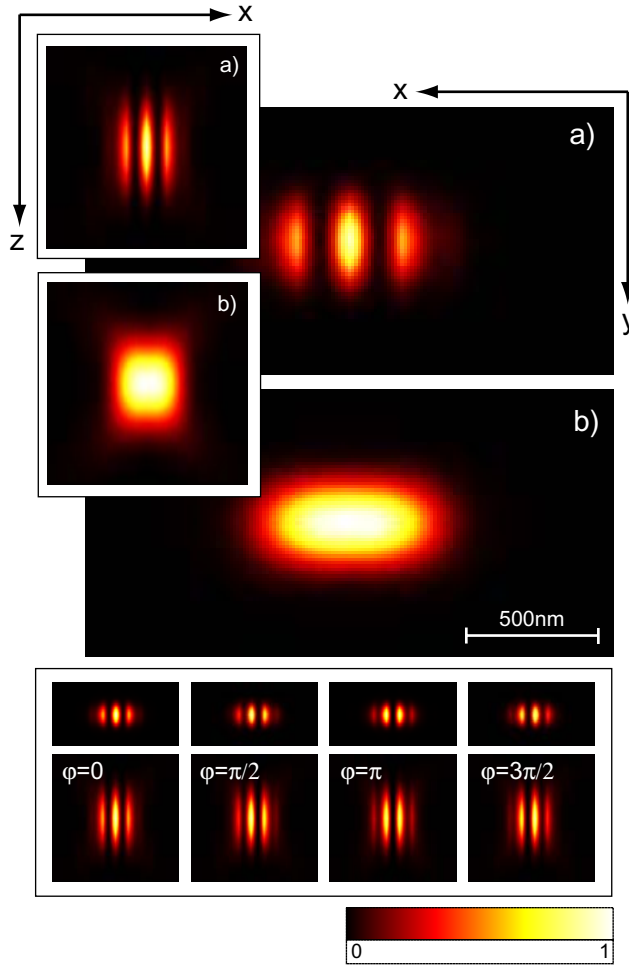
Figure 3.2: *(a) The laterally modulated PSF as created by coherent foci aligned along the x-Axis at a distance of 200nm from each other. Neighboring foci have a phase difference of π and their amplitudes depend on the distance from the center of the envelope and drop off to 1/e² after 400nm. The PSF is shown both in focal plane and in xz-direction. At the bottom the movement of the pattern when moving the foci within the envelope is illustrated. (b) The time average of the moving pattern.*

$L_0 = L_2 = 0$ and $L_1 = 2/\pi$ and for point-like particles and one-photon absorption we therefore expect an amplitude of $2/\pi^2 \simeq 0.2$. Using two photon excitation the amplitude increases by a factor $^{16}/_9$ because the detection volume is effectively reduced due to the quadratic dependence of the excitation probability on the intensity.

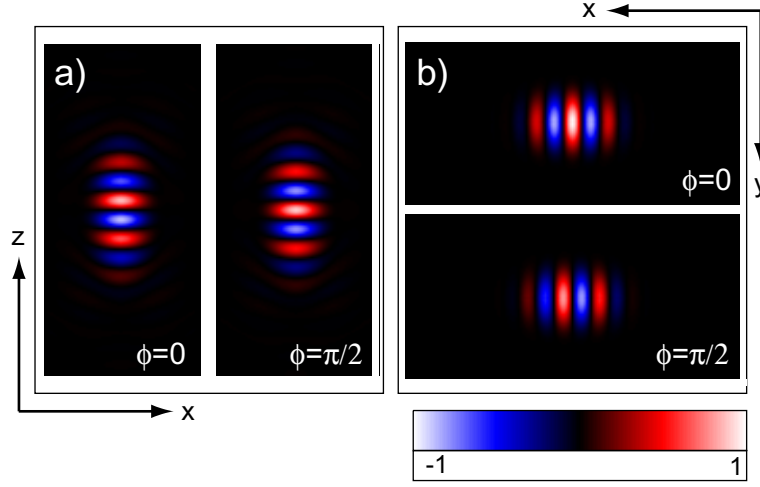If diffusion and flow can only be measured along the optic axis we are limited to

Figure 3.3: *The effective PSFs resulting from combining (a) the axial 4pi pattern shown in figure 3.1 and (b) the lateral pattern illustrated in figure 3.2 with the lock-in detection method. The effect is shown for two phase offsets $\phi$ of the detection modulation.*

applications where the orientation of the sample is known and can be controlled or where a properly oriented sample can be chosen. However, we aim at imaging all the vector components of the flow and thus we need at least two more measurements in linearly independent directions. This requires a way to produce patterns lying in the focal plane. Such patterns have previously been produced by crossing two coherent laser beams in a common focus produced by a single lens.[39,38] With this method, large focal spots with diameters of 100-140$\mu$m were produced. Suitable lateral patterns within a small focal spot are more challenging to find. One possible approach is to superimpose several coherent foci placed along a line with neighboring foci interfering destructively. We will see that such foci can be produced by a single objective lens using techniques already established in multifocal microscopy. Let $\mathbf{E}(\mathbf{r})$ be the E-field of a diffraction limited focus and let $h_{\text{det}}(\mathbf{r})$ be the spatial detection probability. If the position of the foci is $\mathbf{r}_j(t)$ and the amplitude of the beams is $c_j(t)$ the PSF is given by

$$h(\mathbf{r}, t) = \mathcal{C} h_{\text{det}}(\mathbf{r}) \Big| \sum_j (-1)^j c_j(t) \mathbf{E}(\mathbf{r} - \mathbf{r}_j(t)) \Big|^2 \tag{3.63}$$

where $\mathcal{C}$ scales the maximum of $h$ to unity. We line the foci up along the unit vector $\mathbf{e}$ at a distance $d$ from each other and choose a Gaussian dependence of the amplitude on the distance from the center of the envelope with a $1/e^2$ radius $w$. The pattern can be moved by moving the foci along $\mathbf{e}$ and adjusting the

amplitudes in the process. One period is then described by

$$\mathbf{r}_j(t) = (j + t/\Delta t)d\mathbf{e} \tag{3.64}$$

$$c_j(t) = \exp(-2\left|\mathbf{r}_j(t)\right|^2/w^2) \tag{3.65}$$

Figure 3.2 shows the resulting detection volume for $w = 400$nm and $d = 200$nm which can be reasonably well approximated by the first harmonic of the Gaussian model above.

The effective PSFs resulting from lock-in detection with a rectangular modulation function $f_n$ are shown in figure 3.3 for both the lateral and the axial pattern. Because $L_0 = 0$ they oscillate around zero. The positive and negative regions correspond to regions where molecules are excited primarily during times of positive and negative counting by the hardware.

A slight modification of the setup for multifocal 4Pi microscopy[44] would allow to switch between both patterns in the same setup. The details are shown in figure 3.4. The lateral pattern is produced by a rotating microlens disk on which the lenses are arranged parallel to its circumference instead of the usual, more complex arrangement[45]. In order to achieve an interfocal distance of 200nm lenses will also have to be smaller in size and the intermediate optics has to be modified. The detection scheme is simpler than in the imaging case because only a single pinhole is used. The lateral pattern can be oriented at arbitrary angles in the focal plane by rotating the Dove prism.

## 3.7 Simulation of Flow Measurements

In order to validate that the parameters of diffusion and flow can be extracted from the measured correlation curves under realistic conditions the motion of fluorescent particles inside a simulation volume $V$ was simulated. The probability of a particle located at the origin at $t = 0$ moving into an infinitesimal volume element around $\mathbf{r}$ during a time step $\tau$ is given by the spatial part of the concentration correlation function (3.7) which is found by evaluating the Fourier back-transform of $\hat{\alpha}$:

$$\alpha(\mathbf{r}, \tau) = \exp\left(-[\mathbf{r} - \mathbf{v}\tau]^t \mathbf{D}^{-1}[\mathbf{r} - \mathbf{v}\tau]/4\tau\right)\Big/8\sqrt{\pi^3\tau^3 \det(\mathbf{D})} \tag{3.66}$$

Therefore diffusion of a particle during one time step can be simulated by calculating three normal distributed random numbers. Similar simulations have
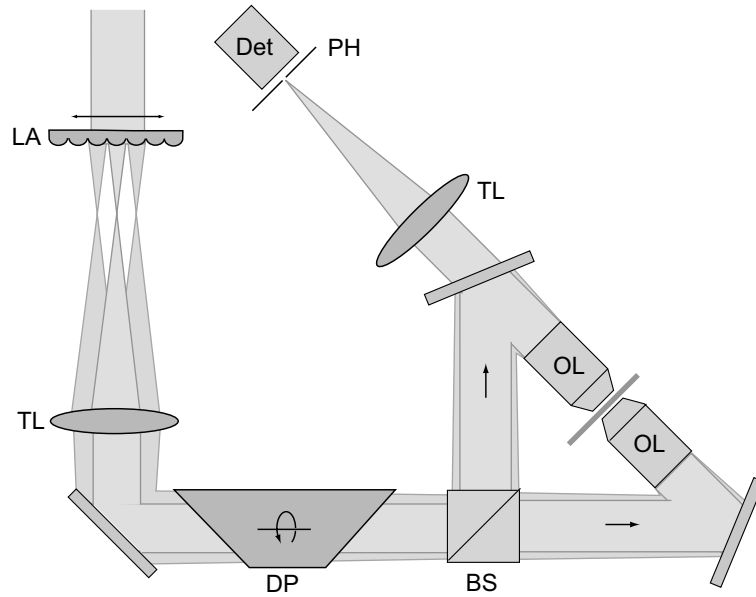
Figure 3.4: *Setup for measuring directional correlation functions in axial and lateral directions. The incident laser beam is split by a beam splitter (BS) into two alternative pathways. One of them passes directly into the 4Pi cavity where two counterprobagating beams are formed and focused onto the same spot by a beam splitter (BS) and two objective lenses (OL). Alternatively a second pathway can be switched on where the beam is split into several, horizontally aligned beamlets by a line of microlenses (LA) which can be moved through the beam profile. When one of the beams in the cavity is switched off this results in a lateral pattern as described in the text. A Dove-prism (DP) is only one of several possibilities to rotate the pattern around the optic axis.*

previously been used to study the quality of data analysis in FCS.[46] In this approach particles leaving the spherical simulation volume where randomly placed on the boundary to keep the concentration constant while other approaches used reflecting boundary conditions.[47] However, in our case particles will preferably enter the volume in the direction of the drift and therefore this method is inadequate. In addition the assumption of a fixed particle number inside $V$ is inaccurate. Its value at a random point in time is Poisson distributed and it exhibits a time correlation dropping off after the time a particle needs to cross the simulation volume. In order to correctly describe these effects, the probability density, $p_{in}(\mathbf{r})$, of a particle from outside the volume appearing at a point $\mathbf{r}$ after a time step $\Delta t$ has to be known. As an approximation we assume particles to be randomly distributed outside the simulation volume, independently of previous

events. Therefore

$$p_{\text{in}}(\mathbf{r}) = \langle C \rangle \int\limits_{\overline{V}} d^3 r' \alpha(\mathbf{r} - \mathbf{r}', \Delta t) \tag{3.67}$$

where $\overline{V}$ is the space outside the simulation volume. Not surprisingly this is proportional to the probability of a particle located at $-\mathbf{r}$ leaving the sample volume during one time step and we can thus simulate $p_{\text{in}}$ in the following way: a Poisson distributed random number of particles with its expectation value given by $\langle C \rangle V$ is randomly distributed in the sample after each step. One time step is simulated only for these particles and all particles which do *not* leave the simulation volume are discarded. The remaining ones are restored at their initial, random position and mirrored about the origin.

Finally the count rates for the three detector channels have to be simulated. If we choose our time steps equal to the hardware time bin in (3.51), the total number of detector counts, $F_e$, is Poisson distributed with mean value

$$\bar{F}_e(t) = Q\Delta t \sum_j h_e(\mathbf{r}_j(t)) \tag{3.68}$$

where the particle trajectories are denoted by $r_j(t)$ and the sum extends over all particles in the simulation volume. The constant $Q$ describes the particle brightness and is defined in (3.3). For each modulated channel some of these counts are added and some are subtracted. The number of positive counts in channel $n$, $F_n^+$, follows the binomial distribution with the following parameters: The number of trials is given by the total number of counts during the time step, $F_e$, and the probability of success is proportional to the fraction of positive contributions to the integral (3.51)

$$h^+(\mathbf{r}, \phi_n) = \int_0^\pi ds h'(\mathbf{r}, s + \phi_n/\omega_L)/[h_e(\mathbf{r})\Delta t] \tag{3.69}$$

where $\phi_n$ is the shift of the rectangular detection modulation. All remaining counts are negative and therefore the signal in channel $n$ is given by $F_n = 2F_n^+ - F_e$. The channel signals can therefore be simulated by generating a single Poisson distributed random number and two random numbers following binomial distributions.

A portable random number generator called ran2[48] which has a period much longer than the amount of calls needed for the simulation of an experiment, was used in the program. At time steps of $10\mu$s the simulations ran about thirty times slower than realtime on a standard 1GHz personal computer. The function $h^+$ was

calculated on a grid which was then used for multilinear interpolation. In all our simulations we assumed a concentration of 40 particles per $\mu$m$^3$ corresponding to a 66nM solution. Tests were made by using an idealized, Gauss-shaped PSF and verifying that the correlation curve converged towards the theoretical prediction (3.31) for long simulation times.

| v | $\bar{D}[\mu$m$^2$/s] | $\bar{v}[\mu$m/s] | $\Delta\phi$ | $A_{\text{lat}}$ | $A_{\text{ax}}$ |
|---|---|---|---|---|---|
| | | T $=$ 100ms | | | |
| 50 | $2.7 \pm 1.3$ | $56 \pm 15$ | $25^o$ | 0.17 | 0.21 |
| 100 | $1.9 \pm 0.5$ | $102 \pm 32$ | $13^o$ | 0.16 | 0.19 |
| 200 | $2.0 \pm 0.5$ | $198 \pm 14$ | $6.2^o$ | 0.15 | 0.19 |
| 500 | $2.5 \pm 0.7$ | $498 \pm 17$ | $3.2^o$ | 0.15 | 0.19 |
| 1000 | $3.5 \pm 1.1$ | $1000 \pm 27$ | $2.3^o$ | 0.15 | 0.19 |
| | | T $=$ 50ms | | | |
| 50 | $1.8 \pm 0.7$ | $64 \pm 25$ | $36^o$ | 0.20 | 0.24 |
| 100 | $1.9 \pm 0.7$ | $107 \pm 25$ | $18^o$ | 0.18 | 0.22 |
| 200 | $2.1 \pm 0.7$ | $203 \pm 22$ | $9^o$ | 0.16 | 0.20 |
| 500 | $2.5 \pm 1.0$ | $506 \pm 34$ | $5.6^o$ | 0.16 | 0.19 |
| 1000 | $3.5 \pm 1.6$ | $1063 \pm 36$ | $3.1^o$ | 0.16 | 0.19 |
| | | T $=$ 25ms | | | |
| 50 | $1.6 \pm 1.0$ | $80 \pm 50$ | $48^o$ | 0.28 | 0.30 |
| 100 | $1.7 \pm 0.9$ | $116 \pm 38$ | $27^o$ | 0.21 | 0.24 |
| 200 | $1.8 \pm 1.0$ | $210 \pm 36$ | $16^o$ | 0.18 | 0.22 |
| 500 | $2.3 \pm 1.3$ | $507 \pm 60$ | $9^o$ | 0.15 | 0.19 |
| 1000 | $3.5 \pm 2.2$ | $1013 \pm 51$ | $4.5^o$ | 0.16 | 0.19 |

Table 3.1: *Results from 1000 simulated flow measurements with randomly oriented flow vectors of a fixed magnitude v and various acquisition times $T$. The average parameter estimates for diffusion constant, $\bar{D}$, flow magnitude, $\bar{v}$, and the amplitudes of $\gamma$ in the lateral and axial direction $A_{\text{lat}}$ and $A_{\text{ax}}$ are shown. The errors reflect the standard deviation of a single measurement and $\Delta\phi$ is the average angle between assumed and fitted flow vector.*

Each flow measurement consisted of three data acquisitions, two with lateral patterns oriented along the x- and y-axis and one with an axial pattern resulting from the 4pi PSF. The correlation curves $\gamma_a$ and $\gamma_s$ were then calculated for each pattern. The data was fitted with the model function (3.59) using a downhill simplex algorithm as introduced by Nelder and Mead[49] for the nonlinear parameters. The diffusion constant varied simultaneously for all curves but the amplitudes of $\gamma$ were allowed to differ for the three patterns. Linear parameters
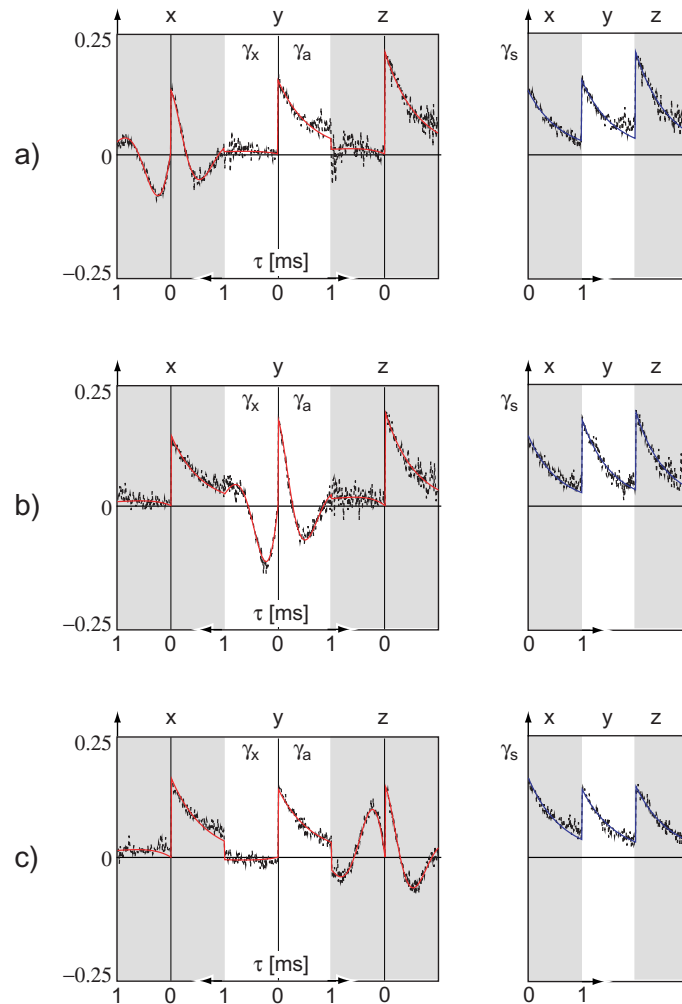
Figure 3.5: *Simulated directional auto- and crosscorrelation functions $\gamma_a$ and $\gamma_x$ resulting from three simulations assuming a diffusion constant of $2\mu\mathrm{m}^2/s$ and a particle flow of $200\mu m/s$ (a) along the x-Axis, (b) along the y-Axis and (c) along the z-Axis. The functions $\gamma_a$ and $\gamma_x$ are plotted right and left of the origin and the results for the three data acquisitions with orientations of the pattern along the x, y and z-direction respectively are shown next to each other. The colored lines are the results of parameter fitting. Clearly only the curves where the pattern was oriented along the direction of flow exhibits the sinusoidal oscillation as predicted by theory. The function $\gamma_s$ presented on the right only depends on the diffusion constant and has the same form in all measurements.*
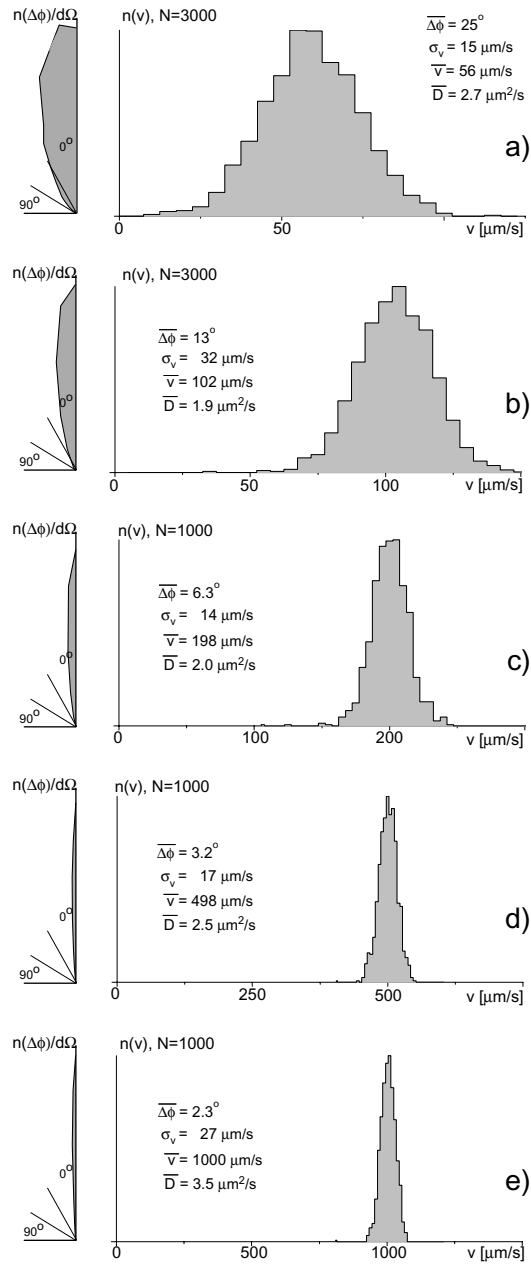
Figure 3.6: *Distribution of measured flow speeds and the angle between actual and measured flow direction in five sets of N simulated experiments. The direction of the flow was arbitrarily chosen in each experiment while the flow speed was kept constant at a) v=50μm/s, b) v=100μm/s, c) v=200μm/s, d) v=500μm/s and e) v=1000μm/s. A diffusion constant of 2μm²/s was assumed. The probability density of the angular error, Δφ per solid angle is plotted on the left.*

were optimized during each step of the iteration using a linear least square algorithm based on the Cholesky decomposition.[48] The statistical significance of each data point in the original correlation curves, $G$ and $G_e$ was assumed equal and instrumental weights were chosen accordingly during fitting. The curves were cut off at the point where $G_e$ dropped below 2% of its maximum. Data analysis using both a logarithmic time scale[42] with 8 channels per octave and a linear time scale produced very similar results. Symmetric normalization[50] was used in all cases. Formulas for statistical noise on correlation data can be found in the literature[51,52,53,46] but introducing an appropriate $\tau$-dependent weighting did not significantly change the results of our fits. Figure 3.5 shows the linear correlation curves resulting from three simulations together with the theoretical curves calculated with the optimized parameters. The flow vector was oriented along each of the cartesian coordinates once in order to illustrate the resulting oscillation of $\gamma$. Because diffusion was assumed equal along each axis $\gamma_s$ drops off at the same rate, regardless of the pattern's orientation. The theoretical curves are the results of fitting the data. For the simple geometry used here fit results were more precise than for arbitrary flow vectors. In order to quantitatively describe the precision of our data analysis a series of measurements was simulated with a randomly oriented flow of constant magnitude. For each measurement the angle between the assumed and fitted flow vector was calculated and recorded together with the fitted speed, diffusion constant and amplitudes. Figure 3.6 shows the result for simulated measurements of 100ms along each axis. Similar runs were conducted using shorter measurement times and the results are listed in table 3.1. Interestingly the amplitude $A_\mathrm{ax}$ for the axial pattern is very close to the predicted 0.2 and the lower amplitude along the lateral direction is due to the lateral pattern not dropping to zero in the minima resulting in a damping of the modulation effect.

Additional simulations were made to test the eligibility of our system for size measurements on particles which are too small or moving too fast for precision imaging. For particles of size $R$ and using the Gauss approximation the model predicts a damping of the directional correlation function's amplitude described by (3.47) and an underestimation of the diffusion constant due to the contribution of the particle size to the matrix $\mathbf{A}(\tau)$ in (3.27). Unlike in conventional FCS[47] the amplitude of $\gamma$ is independent of the concentration of particles and thus the particle size can be extracted without a priori knowledge. The axial pattern of a 4Pi PSF was convolved with spherical particles featuring various diameters in
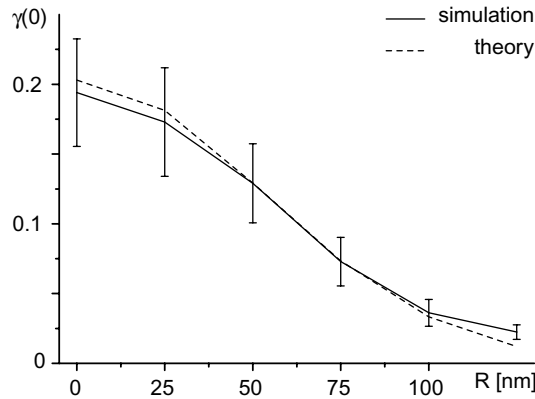
Figure 3.7: *Amplitude of the directional correlation function $\gamma$ extracted from simulations assuming various particle sizes. The theoretical curve is based on an approximation of the spherical particles as Gaussian caps, and neglects all higher harmonics of the pattern modulating the PSF. The error bars represent the standard deviation of individual measurements with an acquisition time of $100ms$.*

order to account for their effect on the effective PSF. While the identical lock-in detection scheme was assumed in these simulations it should be mentioned that time modulation of the pattern is not necessary in this context if diffusion and flow are not to be determined simultaneously. The results are presented in figure 3.7 and show that the method is reliable for particles with sizes up to 100nm. The size of large particles is slightly overestimated as could be expected due to their approximation as Gauss caps.

## 3.8 Measurement of the Diffusion Tensor

The method presented in the previous section could be extended to cases where diffusion is not isotropic but its symmetry axes are oriented along the cartesian coordinates. The estimation of the flow vector might even be acceptable for arbitrary diffusion properties if the measurement time is increased, because the oscillation characteristic for flow along the pattern can be isolated from the curves. However, the model (3.57) contains information about all matrix elements of the diffusion tensor which we would like to extract from our measurements. Data acquisition with patterns along the three cartesian coordinate axes is not sufficient for this task because the resulting correlation functions mainly depend on the diagonal elements of the diffusion tensor and always several of its orientations

would lead to the same form of the curves. Therefore, in order to determine the full tensor, we need correlation curves corresponding to patterns oriented along the bisectors. In the focal plane the image field can be rotated using the Dove prism but in order to tilt the optic axis, the sample would have to be rotated with respect to the lens. Such setups have been proposed for optical tomography [54] but in practice the critical sample alignment and a complicated preparation and mounting process severely complicate such an approach.
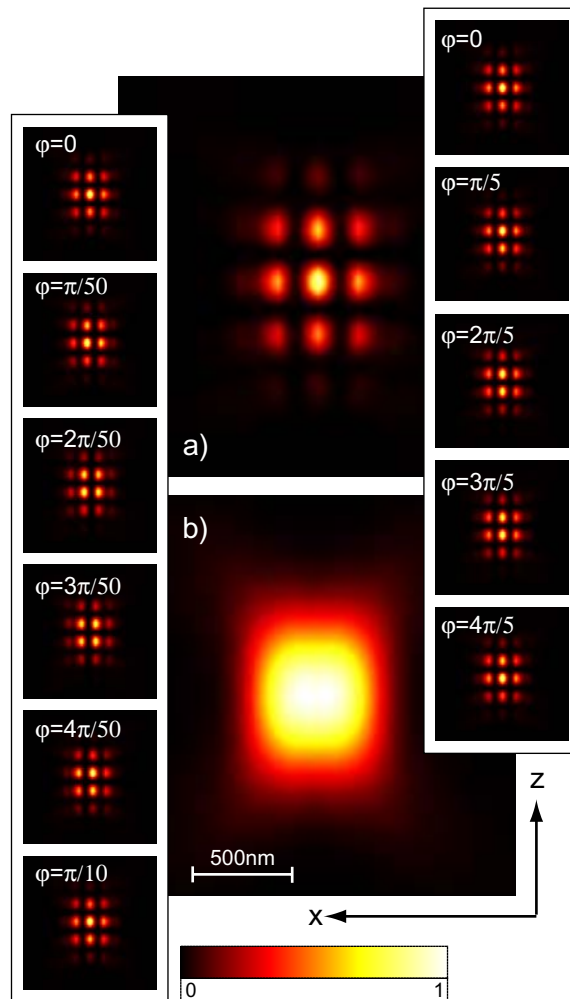


Figure 3.8: *(a) PSF resulting from simultaneously switching on the lateral and the axial pattern generation. The axial and lateral patterns were varied with frequencies $\omega_2 = 9\omega_1/10$ with the periodic variation of the pattern illustrated in the insets. A full period is defined by $\varphi = 2\pi$ and the envelope $h_e$ resulting from time averaging is shown in figure (b).*
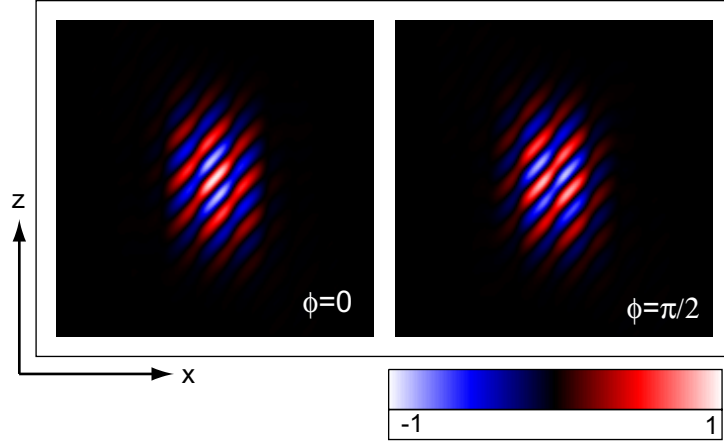
Figure 3.9: *Effective PSF resulting from combining the two-dimensional pattern in figure 3.8 with lock-in detection at a frequency $\omega_1 - \omega_2$. The diagonal structure is used to monitor diffusion along the bisectors of the coordinate system in diffusion tensor measurements.*

As an alternative we switch on both the lateral and the axial pattern in our setup, producing a two dimensional one. The resulting PSF is shown in figure 3.8. We approximate the pattern by the superposition of two periodic patterns defined by the vectors, $\boldsymbol{\kappa}_1$ and $\boldsymbol{\kappa}_2$ and with their time dependence given by the functions $\varphi_{n,1/2}(t)$. We expect a dependence of the correlation function on the diffusion tensor's off-diagonal elements as a result of the patterns diagonal structure. Again, we write the modulations as Fourier sums:

$$h_n\left(\mathbf{r}, \boldsymbol{\kappa}_1, \boldsymbol{\kappa}_2, t\right) = h_e(\mathbf{r}) \sum_{l,j} B_{1l} B_{2j} \exp\bigl(2i\varphi_{n,lj}(t) - 2i\boldsymbol{\kappa}_{lj}^t \mathbf{r}\bigr) \tag{3.70}$$

where we defined

$$\boldsymbol{\kappa}_{lj} = l\boldsymbol{\kappa}_1 + j\boldsymbol{\kappa}_2 \tag{3.71a}$$

$$\varphi_{n,lj}(t) = l\varphi_{n,1}(t) + j\varphi_{n,2}(t) \tag{3.71b}$$

The Fourier transform is obtained using the convolution theorem

$$\hat{h}_n\left(\mathbf{k}, \boldsymbol{\kappa}_1, \boldsymbol{\kappa}_2, t\right) = \hat{h}_e(\mathbf{k}) \sum_{l,j} B_{1l} B_{2j} \exp\left(2i\varphi_{n,lj}(t)\right) h_e(\mathbf{k} - 2\boldsymbol{\kappa}_{lj}) \tag{3.72}$$

and equation (3.19) can then be written as a summation

$$g(\tau) = V_c^2/V^2 \sum_{l,m,j,k} B_{1l} B_{1m} B_{2j} B_{2k} J_{lmjk}(\boldsymbol{\kappa}_1, \boldsymbol{\kappa}_2)$$

$$\times \left\langle \exp\Bigl(2i\varphi_{1,lj}(t) + 2i\varphi_{2,mk}(t+\tau)\Bigr) \right\rangle \tag{3.73}$$

with the volume given by

$$V \simeq V_c B_{20}^2 B_{10}^2 \tag{3.74}$$

Again assuming a Gaussian shape for the envelope the frequency integral can be written as

$$
\begin{aligned}
J_{lmjk}(\boldsymbol{\kappa}_1, \boldsymbol{\kappa}_2, \tau) = \int d^3 k \exp(-\mathbf{k}^t \mathbf{A}(\tau)\mathbf{k}/4 - i\tau\mathbf{k}^t\mathbf{v})/(2\pi)^3 \\
\times \exp\Big(-\boldsymbol{\kappa}_{lj}^t \mathbf{A}\boldsymbol{\kappa}_{lj}/2\Big) \exp\Big(-\boldsymbol{\kappa}_{mk}^t \mathbf{A}\boldsymbol{\kappa}_{mk}/2\Big) \\
\times \exp\Big(\mathbf{k}^t \mathbf{A}(\boldsymbol{\kappa}_{lj} - \boldsymbol{\kappa}_{mk})/2\Big) \quad (3.75)
\end{aligned}
$$

and using equations (B.1) and then (3.42) we find analogously to (3.41)

$$
\begin{aligned}
J_{lmjk}(\boldsymbol{\kappa}_1, \boldsymbol{\kappa}_2, \tau) = g_c(\tau) \exp\Big(i\tau(\boldsymbol{\kappa}_{lj} - \boldsymbol{\kappa}_{mk})^t \mathbf{E}(\tau)\mathbf{v}\Big) \\
\times \exp\Big(-\boldsymbol{\kappa}_{lj}^t \ \mathbf{E}(\tau)(4\mathbf{D}\tau + \mathbf{I}R^2)\boldsymbol{\kappa}_{lj} \ /2\Big) \\
\times \exp\Big(-\boldsymbol{\kappa}_{mk}^t \mathbf{E}(\tau)(4\mathbf{D}\tau + \mathbf{I}R^2)\boldsymbol{\kappa}_{mk}/2\Big) \\
\times \exp\Big(-(\boldsymbol{\kappa}_{lj} + \boldsymbol{\kappa}_{mk})^t \mathbf{E}(\tau)\mathbf{A}(\boldsymbol{\kappa}_{lj} + \boldsymbol{\kappa}_{mk})/4\Big) \quad (3.76)
\end{aligned}
$$

As above we assume that the phases of the pattern vary at constant rates

$$\varphi_{n,lj}(t) = (l\omega_1 + j\omega_2)t + \phi_{n,lj} = \omega_{lj}t + \phi_{n,lj} \tag{3.77}$$

and therefore, if $\omega_1$ and $\omega_2$ and their higher harmonics are distinct, only terms with $m = -l$ and $k = -j$ contribute. In all other cases the same solution is a valid approximation owing to equation (3.45). Putting everything together we obtain

$$
\begin{aligned}
G(\tau)/G_c(\tau) = \sum_{jl} \mathcal{P}_{lj}(\tau)|B_{1l}B_{2j}|^2/(B_{10}B_{20})^2 \\
\times \exp\Big(-4\tau\boldsymbol{\kappa}_{lj}\mathbf{E}(\tau)\mathbf{D}\boldsymbol{\kappa}_{lj}\Big) \exp\Big(2i\big[(\boldsymbol{\kappa}_{lj}\mathbf{E}(\tau)\mathbf{v} - \omega_{lj})\tau + \Delta\phi_{lj}\big]\Big) \quad (3.78)
\end{aligned}
$$

where we defined the phase offset $\Delta\phi_{lj} = \phi_{1,lj} - \phi_{2,lj}$ and the damping function

$$\mathcal{P}_{lj}(\tau) = \exp\Big(-R^2 \boldsymbol{\kappa}_{lj}\mathbf{E}(\tau)\boldsymbol{\kappa}_{lj}\Big) \tag{3.79}$$

Equation (3.78) indeed contains the desired diagonal elements $\boldsymbol{\kappa}_1\mathbf{E}(\tau)\mathbf{D}\boldsymbol{\kappa}_2$ but it depends on several of them simultaneously, which complicates data analysis. However equation (3.78) simplifies significantly when we use frequency filtering. We set $\phi_{n,lj} = \omega_{lj}t$ and choose the frequencies $\omega_1 = 2\pi m/\Delta t$ and $\omega_2 = 2\pi(m - $

$1)/\Delta t$ where $m$ is an arbitrary whole number. When choosing $\omega_L = \omega_1 - \omega_2$ as lock-in frequency only those addends of (3.70) contribute the integral (3.51), for which $\omega_{lj} = q\omega_L$ and therefore

$$q = lm + j(m-1) \quad q \in \mathbb{Z} \tag{3.80}$$

These pairs are given by

$$l = q + \mu(m-1) \quad \mu \in \mathbb{Z} \tag{3.81}$$

$$-j = q + \mu m \tag{3.82}$$

and if we choose $m$ large enough and assume the Fourier coefficients of higher harmonics to become small, we can neglect those contributions with $\mu \neq 0$. The effective PSF is then well approximated by

$$h\left(\mathbf{r}, \boldsymbol{\kappa}, t\right) \simeq h_e(\mathbf{r}) \sum_l B_{1l} B_{2l} L_l \exp\big(il[2\boldsymbol{\kappa}_L^t \mathbf{r} - \phi_m]\big) \tag{3.83}$$

where we defined the diagonal vector selected by the lock-in frequency $\boldsymbol{\kappa}_L = \boldsymbol{\kappa}_1 - \boldsymbol{\kappa}_2$. Figure 3.9 shows the result for the setup proposed here. The diagonal structure is clearly visible and even though the pattern exhibits a secondary structure we will see that the results of simulated measurements are still well described by our theory. In order to introduce a diagonal equivalent to the directional correlation function (3.53) normalization is done with the average signal in the absence of lock-in detection, we introduce independent phase shifts $\phi_1$ and $\phi_2 = \phi_1 + \Delta\phi$ for the two detector channels and define

$$\gamma(\tau, \Delta\phi, \boldsymbol{\kappa}_1, \boldsymbol{\kappa}_2) = G(\tau)/G_c(\tau) - |L_0|^2 \tag{3.84}$$

By picking the correct addends from (3.78) we find

$$\gamma(\tau, \Delta\phi, \boldsymbol{\kappa}_1, \boldsymbol{\kappa}_2) = \sum_{l>0} \mathcal{P}_{-ll}(\tau)|L_l B_{1l} B_{2l}|^2/(B_{10}B_{20})^2$$
$$\times \exp\Big(-4l^2\tau\boldsymbol{\kappa}_L^t \mathbf{E}(\tau)\mathbf{D}\boldsymbol{\kappa}_L\Big) \cos\Big(l[2\tau\boldsymbol{\kappa}_L^t \mathbf{E}(\tau)\mathbf{v} + \Delta\phi]\Big) \tag{3.85}$$

For data fitting we will assume that the higher harmonics can be neglected. The amplitude we expect is given by $\pi/2$ times the product of the average lateral and axial amplitudes which corresponds to approximately 0.045 in our case. When measuring the diffusion tensor three additional curves are recorded as compared to flow measurements. One measurement now consists of six data acquisitions with lateral patterns along the x- and y-axis as well as along the xy-bisector,
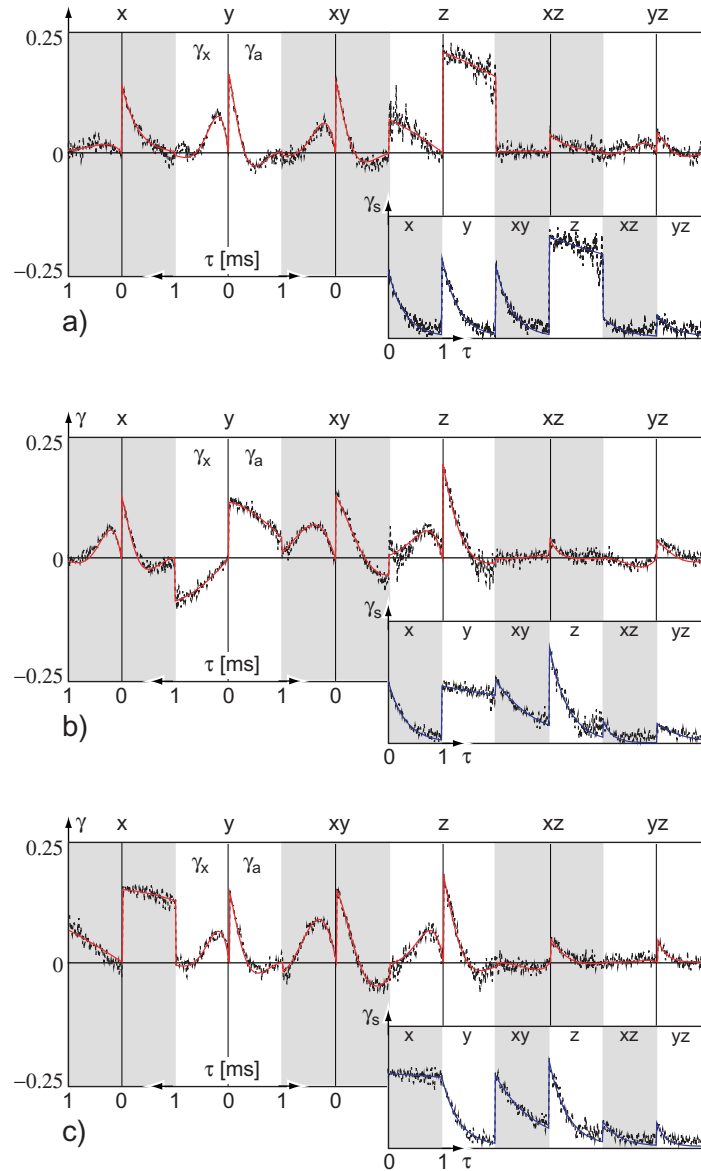
Figure 3.10:  *Simulated data and fitted curves for diffusion tensor measurements. All six data acquisitions are shown next to each other for each of the measurements. Diffusion was assumed exclusively (a) in the xy- (b) in the xz- and (c) in the xz-plane but an arbitrary flow vector was chosen for each of the measurements. The diffusion constant was $4\mu m^2/s$. The function $\gamma_s$, which is plotted in the insets, illustrates the absence of diffusion in the direction normal to the diffusion plane.*

| | $\bar{D}_{0/1}[\mu\mathrm{m}^2/\mathrm{s}]$ | $\bar{D}_2[\mu\mathrm{m}^2/\mathrm{s}]$ | $\Delta\phi$ | $A_{\mathrm{lat}}$ | $A_{\mathrm{ax}}$ | $A_{\mathrm{diag}}$ |
|---|---|---|---|---|---|---|
| (a) | $3.6 \pm 0.5$ | $0.4 \pm 0.4$ | $31^o$ | 0.14 | 0.18 | 0.038 |
| (b) | $0.3 \pm 0.3$ | $3.5 \pm 0.1$ | $27^o$ | 0.15 | 0.19 | 0.038 |

Table 3.2: *Results from simulated diffusion tensor measurements with 200 randomly oriented tensors for (a) diffusion in a plane and (b) diffusion in only one direction with $D = 4\mu\mathrm{m}^2/s$. The average parameter estimates for the diffusion constant, $\bar{D}$, and the amplitudes of $\gamma$ in the lateral, axial and diagonal direction $A_{\mathrm{lat}}$ ,$A_{\mathrm{ax}}$, $A_{\mathrm{diag}}$ are shown. The errors reflect the standard deviation of a single measurement and $\Delta\phi$ is the average angle between assumed and fitted tensor orientation.*

an axial pattern along the z-axis and two-dimensional patterns in the xz- and the yz-planes. An acquisition time of 400ms was assumed for each of the patterns. Data fitting was accomplished by simultaneously fitting the data from all six recordings of a measurement using the model (3.56). Figure 3.10 shows 3 exemplary simulation runs. The diffusion tensor was oblate simulating diffusion only parallel to a plane, e.g. within or on the surface of a biological membrane. Diffusion was assumed once in the xy-, the xz- and yz planes illustrating the influence of the tensor's orientation on the correlation curves.

In order to quantify the precision of such measurements a series of simulations with randomly oriented diffusion tensors and flow vectors was run. In addition to
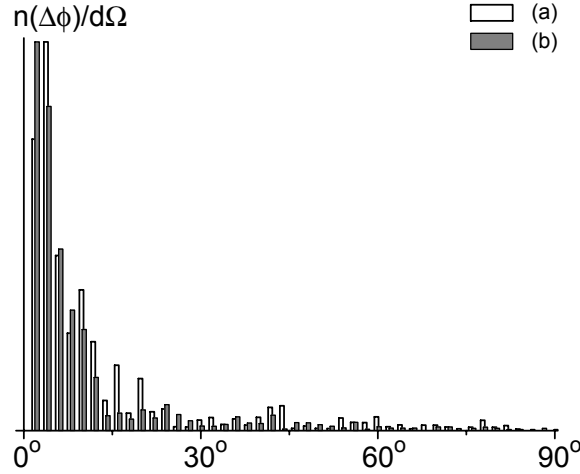


Figure 3.11: *Distribution of the angle $\Delta\phi$ between assumed orientation of the diffusion tensor and the guess based on simulated correlation data. The frequency of occurrence has been plotted per solid angle and values are given for (a) diffusion in a plane and (b) diffusion in only one direction.*

diffusion in a plane, a prolate tensor was assumed in a second set of simulations, imitating e.g. diffusion along microtubule or filaments. The results are listed in table 3.2. Clearly, our system distinguishes planar and linear diffusion from the isotropic case and simultaneously identifies particle drift. The amplitude for the xz- and yz-curves is lower than predicted by the Gauss approximation due to the imperfections of the pattern. Figure 3.11 illustrates the quality of the estimates for the orientation of the tensor. Obviously, the scheme proposed has the potential to image preferred directions of diffusion, however the average error of approximately $30^o$ is still quite large and automatic fitting failed in about 10% of the cases. These problems could be solved by a more elaborate data analysis, based on the comparison of several fitting attempts with different initial guesses for the parameters.

## Chapter 4

# Monitoring Energy Transfer Using STED

Stimulated emission depletion (STED) microscopy is the first far-field technique with a resolution that is not fundamentally limited by the diffraction of light. Its basic principle is to stop fluorescence from molecules that are not located in the center of the focal spot. This is accomplished by employing pulsed excitation and quenching the excited state of the dye with a second, red-shifted pulse that arrives a short time afterwards. Using diffraction techniques the focal intensity of red light is distributed around the excitation maximum while ensuring zero intensity in an interference minimum in the center. When increasing the power of the STED beam, fluorescence can be almost completely quenched at places where the intensity of the red light reaches only a fraction of its maximum value in the focal area. Therefore fluorescence is effectively hindered even in the immediate vicinity of the excitation maximum which ideally remains unaffected due to the interference minimum. Thus theoretically, the resolution can be improved indefinitely by increasing the strength of the STED beam.

If the STED beam forms a regular focus, which is then aligned with the excitation focus, a STED microscope turns into a tool for pump-probe experiments at arbitrary spots of the sample. Because the STED beam quenches fluorescence only from dyes with are in their excited state when the pulse arrives, the reduction of fluorescence effectively monitors the population of that state. By changing the temporal offset between the two beams its time evolution during an excitation cycle can be analyzed.[55]

Fluorescence resonant energy transfer (FRET) is the nonradiative transfer of

energy from a donor to an acceptor molecule by a weak dipole-dipole coupling mechanism. The FRET efficiency is the probability that an excited donor actually transfers its energy to the acceptor before being quenched or decaying radiatively. It was predicted by Förster to depend on the sixth power of the distance, $R$ between donor and acceptor[56], and is given by $E = [1 + (R/R_0)^6]^{-1}$. The constant $R_0$ is the Förster radius, the distance at which 50% efficiency is reached. It depends on the spectral overlap integral of the donor's fluorescence spectrum with the excitation spectrum of the acceptor, $J(\lambda)$, the fluorescence quantum yield of the donor, $\phi_d$, the refractive index of the medium, $n$ and an orientational factor $\kappa^2 = [cos\theta_t - \cos\theta_d \cos\theta_a]^2$ where $\theta_t$ is angle between the transition moments and $\theta_a$ and $\theta_d$ are the angles between the separation vector of their centers and the acceptor- and donor transition moment, respectively. With $J(\lambda)$ in $M^{-1}cm^{-1}nm^4$. we have

$$R_0 = [8.79 \cdot 10^{-5} J(\lambda)\phi_d \kappa^2/n^4]^{1/6} \quad [\text{Å}] \tag{4.1}$$

Thus, if relative orientations are isotropic or known, a FRET pair can serve as a spectroscopic ruler in biological systems owing to the strong dependence of the transfer efficiency on the distance between the dyes. In principle, FRET efficiencies are most easily measured by comparing the amount of donor and acceptor fluorescence in a calibrated system. For this, the ratio of the quantum yields of donor and acceptor has to be known. An additional problem is the contribution from uncoupled donor molecules which reduces the measured transfer efficiency. While this 'zero peak' can be literally sorted out in single molecule experiments[57], its control in bulk measurements, especially in complex environments, is difficult. Alternatively the fluorescence decay of the donor can be monitored. However the rate is influenced by many mechanisms other than FRET and those pairs with most effective transfer contribute least to the donor signal making analytis difficult or impossible.

These problems can in principle be overcome by monitoring the excitation rate of the acceptor directly. Under pulsed illumination, the rate at which acceptor fluorescence increases after excitation of the donor is determined by the FRET rate. At high transfer efficiencies this increase is too fast to be detected in traditional lifetime imaging.

Because a STED microscope inherently monitors the excited state of the quenched dye it has both the required temporal resolution and the imaging capabilities to carry the method back into biological systems. In this chapter these possibilities are evaluated on a model system.

## 4.1   Theory

We only consider the electronic ground state and the first excited state for both
donor and acceptor and neglect effects originating from vibrational relaxation.
The system has then 4 states corresponding to the following configurations: Both
molecules are excited ,$D^*A^*$, only the donor is excited ,$D^*A$, only the acceptor is
excited ,$A^*D$, and both molecules are in the ground state ,$DA$. They are shown in
figure 4.1 together with the relevant transition rates. The rate of energy transfer
is related to the FRET efficiency by the formula $E = k_t/[k_t + k_d]$. The intensity
of donor fluorescence, $I_d$ and acceptor fluorescence, $I_a$ is measured in two spectral
channels. Let $q_{d,a}$ be the product of quantum yield and collection efficiency for
donor and acceptor, thus denoting the probablility that a photon is registered in
the appropriate channel when a dye decays into its ground state. Usually some
donor fluorescence also leaks into the acceptor channel and vice versa and we
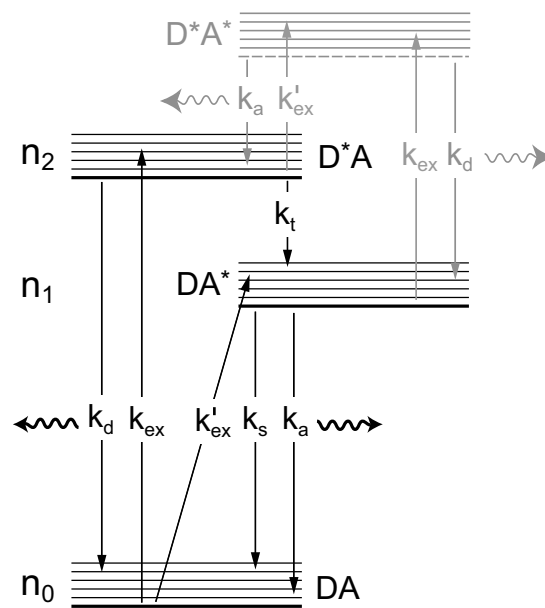


Figure 4.1:  *Simplified Jablonski diagram of two dyes coupled by FRET. The 4 states
correspond to the permutations of excited and relaxed donor and acceptor. The case of
both dyes being excited is neglected in the formulae and depicted in gray. The remaining
states are labeled $n_0$, $n_1$ and $n_2$ and $k_d$ and $k_a$ are the decay rates of the excited state of
donor and acceptor respectively; $k_{ex}$ are excitation rates and $k_s$ is the rate at which light
quenching of the excited acceptor takes place. Finally $k_t$ is the rate of Förster transfer
between the dyes.*

denote their fractions by $\delta_d$ and $\delta_a$. If we are far from saturation and the ratio between unwanted, direct acceptor excitation and donor excitation is given by $\xi$ the signal in the channels is given by

$$I_a = C[(E + \xi)q_a + (1 - E)q_d\delta_d] \tag{4.2a}$$

$$I_d = C[(E + \xi)q_a\delta_a + (1 - E)q_d] \tag{4.2b}$$

where $C$ is a scaling constant and with $\gamma = q_a/q_d$ the transfer efficiency is

$$E = [1 + \gamma(I_d - I_a\delta_a)/(I_a - I_d\delta_d - Cq_a\xi(1 - \delta_a\delta_d))]^{-1} \tag{4.3}$$

Please note that for zero cross-talk ($\delta_a = \delta_d = 0$) and if only the donor is excited ($\xi = 0$) this simplifies to

$$E = [1 + \gamma I_d/I_a]^{-1} \tag{4.4}$$

Spectral measurements of FRET efficiencies are based on this formula. The $\delta$'s are easily determined by calibration measurements. The amount of fluorescence from direct acceptor excitation can be controlled by careful selection of the excitation wavelength or it must be estimated. The main source of inaccuracy is the factor $\gamma$, which is often unknown because quantum efficiencies are difficult to determine and depend on the dye's microenvironment. However it can in principle be measured directly in the sample by bleaching some of the acceptors between two consecutive measurements. For bleached acceptors $E$ becomes zero and we have

$$q_a/q_d = -(\Delta I_a + \delta_d\Delta I_d)/(\Delta I_d + \delta_a\Delta I_a) \tag{4.5}$$

where $\Delta I_a < 0$ and $\Delta I_d > 0$ is the change of the signals after acceptor bleaching. Of course, this approach renders the sample unusable for further analysis unless diffusion exchanges molecules. Even without previous bleaching, single donor molecules usually contribute to the signal owing to unwanted bleaching of excess labeling. In single molecule experiments these contributions can be literally sorted out[57] but in bulk measurements controlling this error is one of the most challenging tasks.

Our goal is to solve this problem by directly monitoring the excitation of the acceptor through energy transfer. Let us therefore consider the time evolution of the system after initial excitation. We now assume pulsed excitation and that all molecules are in their ground state before each excitation pulse. The pulse is assumed to be very short as compared to the other transition rates. At sufficiently low intensities saturation is avoided and a fraction $\xi_d = k_{\mathrm{ex}}\Delta t = \Phi\sigma\Delta t$ of donor

molecules is excited during each pulse where $\sigma$ is the excitation cross section, $\Phi$ is the average density of the photon flux during the pulse and $\Delta t$ is the pulse length. Similarly a fraction $\xi_a = k'_{\mathrm{ex}}\Delta t = \xi\xi_d$ of acceptor molecules is excited. If $\xi_a, \xi_d \ll 1$, contributions from systems where both dyes are initially excited are negligible and we therefore disregard the state $D^*A^*$ in our considerations. In the absence of STED the time evolution of the states is then described by the equations

$$dn_2(t)/dt = -[k_d + k_t]n_2(t) \tag{4.6a}$$

$$dn_1(t)/dt = k_t n_2(t) - k_a n_1(t) \tag{4.6b}$$

and if the excitation pulse is at $t = 0$ the solution is

$$n_2(t) = \xi_d \exp(-[k_d + k_t]t) \tag{4.7a}$$

$$n_1(t) = (\xi_a + \eta\xi_d)\exp(-k_a t) - \xi_d\eta\exp(-[k_d + k_t]t) \tag{4.7b}$$

where $\eta = k_t/[k_d + k_t - k_a]$. Note that at $t = 0$ we have $dn_1/dt = \xi_d k_t$ and therefore the excited state of the acceptor is initially filled exactly with the FRET rate, as could be expected. The total signals are still given by (4.2b).

If the sample is irradiated with a STED pulse, which is short compared to the transition rates, a fraction $\epsilon$ of all excited acceptor molecules is quenched. $\epsilon$ is called the STED efficiency[58] and if $k_s$ is faster than the other transition rates but slow enough for vibrational relaxation to avoid re-excitation it is given by $\epsilon = 1 - \exp(-k_t\Delta t) = 1 - \exp(-\sigma_t\Phi\Delta_t)$ where $\Delta t$ is the pulse duration, $\Phi$ the density of the photon flux and the $\sigma_t$ the cross section for stimulated emission of the acceptor. Assuming that the donor is not quenched and the pulse arrives at $t = \tau$ the signal in the acceptor channel is given by

$$I_a(\tau) = I_a - C\epsilon q_a n_1(\tau) \tag{4.8}$$

and here we will measure the time dependent STED efficiency

$$\epsilon(\tau) = 1 - I_a(\tau)/I_a = \beta\exp(-k_a\tau) - \alpha\exp(-[k_d + k_t]\tau) \tag{4.9}$$

with the fraction of direct acceptor excitation given by $\xi = \eta(\beta - \alpha)/\alpha$. Our experiments will aim at extracting $k_t + k_d$ from $\epsilon(\tau)$. For large transfer efficiencies ($k_t \gg k_d$) this is a direct measurement of the FRET rate, in other cases $k_d$ has to be determined independently.
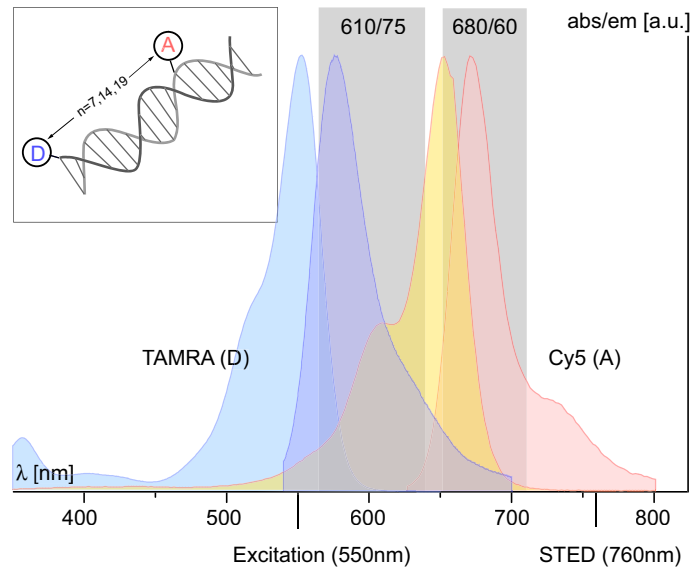
Figure 4.2: *Schematic of the DNA-n constructs used (inset). The donor (TAMRA) was always attached to the 5' end the first oligomere while the acceptor (Cy5) was bound to the nth base on the complementary oligomere. The absorption and emission spectra of the donor (TAMRA) and acceptor (Cy5) are shown along with the detection windows of the band-pass filters used to separate donor and acceptor fluorescence. Below the wavelengths of excitation and STED beam are marked.*

## 4.2 Materials and Methods

Because the goal of the experiments was to verify that STED can be used to identify FRET inside samples imaged by a microscope, the setup was based on a custom built stage scanning confocal fluorescence microscope. A Ti:Sapphire system (Coherent, Santa Clara, CA, USA) delivered a train of laser pulses of 76MHz at 760nm and some of the red light was converted into green 550nm light in an optical parametric oscillator (APE, Berlin, Germany). The green (excitation) pulses were 250fs long while the red (STED) pulses were stretched to 13-15ps by down-chirping them in a holographic grating decompressor. Both beams passed a liquid crystal laser power controller LPC (Cambridge Research & Instrumentation, Woburn, MA, USA) which was used to adjust the excitation and STED intensities and removed noise from the laser signal. The time lag between excitation and STED pulses was controlled with sub-picosecond precision by moving a retro reflector mounted on a linear stage (Owis, Staufen, Germany). The beams were focused through pinholes in order to improve the quality of the wavefronts.
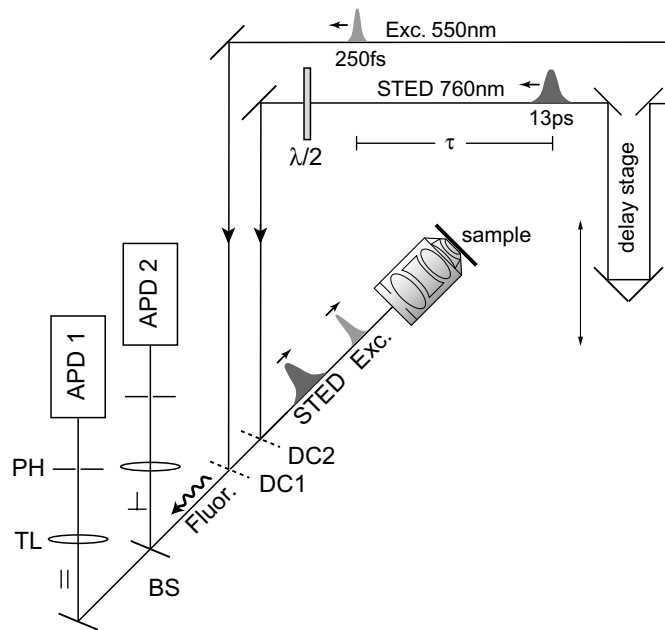
Figure 4.3:  *STED-microscopical setup used for monitoring FRET. The dichroic mirror (DC1 and DC2) combine the two beams and transmit fluorescence from the sample which is split into its polarization components by a polarizing beam splitter cube (BS) and focused on the opening of an APD's fibre which acts as a pinhole (PH). The polarization of the STED beam can be rotated using a $\lambda/2$ plate.*

Two dichroic mirrors, one being transparent for excitation light and fluorescence (700DCSX, Chroma, USA) and one transmitting only fluorescence (650DCWB, Chroma, USA) were used to join their pathways and separate them from fluorescence. The beams were then focused into the sample using a NA=1.2 63x water immersion lens (Leica, Wetzlar, Germany). Both beams could be independently switched on and off by automatic shutters and the polarization of the STED beam could be changed using a $\lambda/2$-plate. The beam diameter of the excitation light was larger than the back-aperture (7.7mm) of the lens producing a diffraction limited spot. The STED beam was narrowed to 3mm by an aperture enlarging the focus almost 7-fold and ensuring a virtually uniform intensity throughout the confocal detection volume. Typical laser powers in the sample were $< 1\mu$W of green and 2-3mW of red light. Fluorescence polarized parallel and perpendicular to the excitation beam was separated by a polarizing beam splitter and detected separately by focusing it onto the opening of an Avalanche Photo Diode's (APD, EG&G Vandreuil, Quebec, Canada) input fibre with a tube lens. The fibre di-

ameter ($62.5\mu$m) served as a pinhole for confocal detection and corresponded to 310nm in the sample which is less than the size of the Airy disk. Band pass filters were used to select donor and acceptor fluorescence. (HQ680/60 for the acceptor, HQ610/75 for the donor, both Chroma, USA) Time-correlated single photon counting (TCSPC) was accomplished simultaneously in both polarization channels on a personal computer using an SPC-535 ISA-card (Becker & Hickl GmbH, Berlin, Germany) and a custom acquisition and analysis software 'Imspector' for multiparameter microscopy[59] that allowed for online analysis and control, synchronization and readout of most components including an xyz-stage for scanning the sample, the LPCs, linear stage and shutters. The time dependent STED efficiency was measured by scanning the time offset between excitation and STED pulse using the linear stage. The change to the path of the red light altered its transmission through the pinhole by up to 15% and this effect was compensated during the measurement by using the LPC to keep the focal intensity at a constant level. Acceptor fluorescence was detected in both polarization directions and the signal $I = I_\parallel + 2I_\perp$ was calculated for each time offset.

Doubly labeled double stranded DNA was used as a model system because of its known structure. The FRET pair had to be chosen such that acceptor fluorescence could be detected between the excitation and STED wavelengths and the influence of the STED beam on the donor was minimized. The dyes TAMRA (6-isomer, donor, Molecular Probes) and Cy5 (acceptor, Amersham) met these criteria (see figure 4.2) and were chosen due to the large Förster radius ($\sim$53Å) for energy transfer between these dyes. In all experiments TAMRA was attached to the 5'-end of the 29mer 5'-CTC TTC **A**GT TCA C**A**G TCC **A**TC CTA TCA GC-3' with a 5'-aminomodifier ($C_6$). For the DNA-n (n=7;15;19) constructs Cy5 was attached to a thymidine residue via a $C_6$-linker and an aminomodifier (Amino Modifier C6 dT, Glenresearch) at position $n$ on the complementary oligomer. The oligonucleotides were double HPLC purified. All synthesis was done by IBA GmbH NAPS (Göttingen, Germany). The strands were hybridized by mixing them 1:1 in a buffer containing 180mM NaCl, 12mM Na-citrate and $25\mu$M MgCl$_2$ (pH 7.5) and cooling them slowly from 95 to 20$^\text{o}$C. Donor-only and acceptor-only labeled molecules were made by hybridizing with the unlabeled complement. For measurement a sodium phosphate buffer containing 180mM NaCl, and 10mM NaH$_2$PO$_4$/Na$_2$HPO$_4$ (pH 7.5) was used, the concentration of DNA molecules was adjusted to $9\mu$M and microscope slides with a dent were used to minimize the effects of adhesion on the walls.

## 4.3 Results and Discussion

In order to reduce the error due to low frequency laser noise the fluorescence intensity with and without irradiation by the STED beam was recorded alternatingly for 160ms resulting in two values, $I_1$ and $I_0$. The average of 8 such measurements was taken at each time offset and the time dependent STED efficiency $\epsilon = 1 - I_1/I_0$ was calculated. For $\tau < 0$ negative values of $\epsilon$ were obtained. This means that a STED pulse arriving before the excitation pulse actually enhanced fluorescence and was observed for both acceptor-only and doubly labelled DNA. One possible reason is that the red light influences the process of trans-cis isomerization of Cy5, reducing the population of the non-fluorescent cis-state. The enhancement did not show any $\tau$ dependence between -550ps and -20ps and was therefore assumed approximately constant over the 13ns between pulses. Therefore $I_1/I_0$ was normalized to unity at $\tau < 0$ before further analysis. For each DNA construct curves for acceptor-only molecules were recorded in order to extract the decay rate $k_a$. This value agreed well with the lifetimes extracted from TCSPC for only the parallel detection channel, as expected. The curves for doubly-labelled molecules were then fit with equation (4.9), keeping $k_a$ fixed. Such measurements are shown in figure 4.4 together with the fits for all three DNA constructs. For the DNA-7 construct an additional rate had to be introduced in order to describe the data. In principle this would be evidence for at least one sub-population with a different FRET rate, maybe due to a different relative orientation of donor and acceptor but we will see below that an artefact can not be ruled out. The donor lifetime was measured using TCSPC on donor-only labelled samples. The decay curves could be fit by a double exponential and the faster decay rate, which had a 5-6 times stronger amplitude was used here. Values for all constructs are listed in table 4.1 and the FRET efficiencies calculated from $k_t$ compare well with those found in single molecule experiments for similar DNA constructs.[57]

However, the values obtained for the fraction of direct acceptor excitation, $\xi$ are much higher than expected from the spectra and measurements with acceptor-only labelled DNA and the origin of fluorescence enhancement at $\tau < 0$ is not yet identified. In addition the second rate for DNA-7 and the rates obtained for DNA-14 and DNA-19 are not too fast to be influenced by the decay of rotational anisotropy making a reliable interpretation difficult.

In order to remove these uncertainties the STED intensity would have to be chosen far from saturation and additional measurements with the polarization of
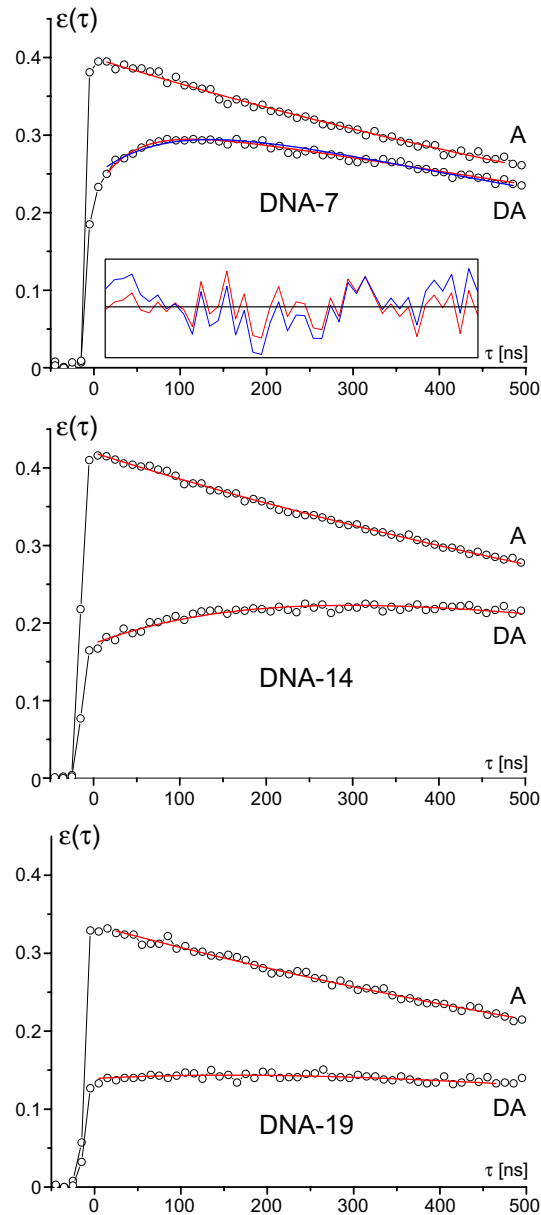
Figure 4.4: *The dependence of the STED-efficiency $\epsilon$ for acceptor-only and doubly labeled (a) DNA-7, (b) DNA-14 and (c) DNA-19 construct on the time delay between excitation and STED pulse. Effectively $\epsilon$ monitors the excited state of the acceptor and thus its 'filling' after excitation of the donor due to energy transfer. The offset is due to direct excitation of the acceptor. The colored curves are the result of fits with equation (4.9). For DNA-7 a fit with two transfer rates,which describes the data much better, is also shown and the residuals are compared in the inset.*

| | $k_a$ [1/ns] | $k_d$ [1/ns] | $k_t$ [1/ns] | $\xi$ | E | $E_{\mathrm{den}}$ |
|---|---|---|---|---|---|---|
| DNA-7 | 0.87 | 1.22 | 23 | 0.95 | 93 | 95 |
| | | | 2.8 | | 63 | |
| DNA-14 | 0.84 | 1.21 | 2.5 | 0.76 | 68 | 72 |
| DNA-19 | 0.89 | 1.26 | 1.3 | 0.78 | 51 | 42 |

Table 4.1: *Acceptor decay rate, $k_a$ and rate of energy transfer, $k_t$, extracted from the time dependent STED efficiency using equation (4.9). The rate of donor decay through channels other than FRET, $k_d$ was obtained from TCSPC measurements. $\xi$ is the fraction of direct acceptor excitation. The FRET efficiency E calculated from $k_t$ and $k_d$ is compared to the values obtained by Deniz et al. for the same distance between the dyes.*

the red beam rotated by $90^o$ are needed. Indeed, rotating the polarization of the STED beam using the $\lambda/2$ plate resulted in significantly lower STED efficiencies and different time constants. But in such measurements the rotational symmetry around the polarization direction of the exciting beam is broken and either fluorescence has to be detected in all three polarization directions or further assumptions about the FRET pairs have to be made. However, this is a purely spectroscopical task and for an application at low signal in a complex environment, possibly inside a biological specimen this is inadequate. Nevertheless figure 4.4 and the data from 4.1 show that the method can identify energy transfer and for simpler systems quantitative analysis might be possible also inside a microscope.

# Chapter 5

# Summary and Outlook

In this work the prospect of applying techniques which were originally established in point spread function engineering to spectroscopical imaging was explored. The first part was dedicated to the description of the focal intensity pattern in the Fourier domain, taking into account the vectorial nature of light and arbitrary manipulations of the wavefront before it enters the lens. A simple integral solution for the excitation OTF of both a single lens and a 4Pi setup was presented, suitable for fast and precise numerical calculations. It was used to calculate an upper bound of 3K for focal heating under typical conditions in a two photon microscopes. Because the formalism allows for arbitrary modifications of the wavefront, can be applied for the analysis of aberrations and the design of new pupil filters.

The combination of 4Pi microscopy with fluorescence correlation spectroscopy was examined next. Theoretical analysis took place in the Fourier domain using the OTF. In order to exploit its full potential, the approach was extended to arbitrary periodic patterns modulating the enveloping PSF. The fluid model was changed to account for anisotropic diffusion and directed particle drift. It was shown, how the comparison of correlation measurements with and without modulation of the PSF can separate information about particle movement from fluctuations due to internal dynamics of the fluorescent entities. Approximating the envelope of the PSF by a Gaussian, an analytical solution for the predicted correlation curves was found. An experimental method based on a multifocal 4Pi setup, which forms patterns of various orientations in its focus was then proposed and theoretically investigated. Simulated measurements, using PSFs calculated from diffraction theory showed that the flow vector can be determined from three correlation curves with different pattern orientations and that not more than 6

correlation measurements are needed to fully assess anisotropic diffusion.

Finally STED microscopy was used to monitor Förster energy transfer between two molecules. An appropriate experiment was set up and TAMRA and Cy5 attached to double-stranded DNA served as a test system. Indirect excitation of the acceptor through energy transfer from the donor was clearly visible when monitoring the acceptor's excited state using stimulated emission. Even though quantitative analysis was difficult, this finding is significant because a new method for identifying FRET in a microscopical environment has been established. By detecting fluorescence in all three polarization directions in a dedicated setup and careful spectroscopical analysis the uncertainties remaining in the data interpretation could be avoided. The original setup could then be calibrated for a specific FRET pair allowing for the quantification of energy transfer based on the comparison of FRET efficiencies for a few time offsets between excitation and STED pulse. This technique can be readily applied in every STED microscope originally designed for resolution improvement.

The experimental realization of 4Pi microscopy with fluorescence correlation spectroscopy is already under way. Anisotropic diffusion is present in biological systems whenever sub-structures designate a direction. As an example it has been found in cell dendrites, where microtubules hamper diffusion perpendicular to their orientation.[34] In these systems patterned correlation spectroscopy will deliver information about the orientation of the sub-structure not assessable by established methods.

# Appendix A

# Complex Fluids

## A.1 General Theory

We assume that the fluid is formed by particles, be it molecules or larger structures like fluorescent beads or macromolecules. Different types of particles or particles in different states exist in the fluid. Let there be an average of $\langle N_j \rangle$ particles of type $j$ with their trajectories given by $r_m^{(j)}(t)$. The particle numbers may vary during time due to chemical or photophysical reaction. We will later consider the limit of an infinite volume while keeping the average concentrations, $\langle C_j \rangle = \langle N_j \rangle / V$, constant. The time dependent, local particle density of type $j$ is given by

$$C_j(\mathbf{r}, t) = \sum_m \delta(\mathbf{r} - \mathbf{r}_m^{(j)}(t)) \tag{A.1}$$

Please note that this and all subsequent sums are over all particles that exist of the type at the given time. The statistical information about the dynamical properties of the fluid's structure is contained in the density-density time correlation function given by

$$H_{jk}(\mathbf{r}, \mathbf{r}', \tau) = \left\langle C_j(\mathbf{r}' + \mathbf{r}, t + \tau) C_k(\mathbf{r}', t) \right\rangle \Big/ \langle C_k \rangle \tag{A.2a}$$

$$= \left\langle \sum_{m,n} \delta(\mathbf{r}' + \mathbf{r} - \mathbf{r}_m^{(j)}(t + \tau)) \delta(\mathbf{r}' - \mathbf{r}_n^{(k)}(t)) \right\rangle \Big/ \langle C_k \rangle \tag{A.2b}$$

which is the averaged probability density of finding a particle of type $j$ at a place $\mathbf{r}' + \mathbf{r}$ after a time-span $\tau$ given that a particle of type $k$ was initially at position $\mathbf{r}'$. If we remove the dependence on the origin $\mathbf{r}'$ by averaging over all space, we obtain a generalization of the time- and space-dependent distribution function

introduced by van Hove. By simple substitution we can carry out the integral

$$H_{jk}(\mathbf{r}, \tau) = \int d^3 r' \left\langle C_j \left(\mathbf{r}' + \mathbf{r}, t + \tau\right) C_k \left(\mathbf{r}', t\right) \right\rangle \Big/ \langle C_k \rangle V \tag{A.3a}$$

$$= \int d^3 r' \left\langle \sum_{m,n} \delta(\mathbf{r}') \delta(\mathbf{r}' + \mathbf{r} - \mathbf{r}_m^{(j)}(t+\tau) + \mathbf{r}_n^{(k)}(t)) \right\rangle \Big/ \langle N_k \rangle \tag{A.3b}$$

$$= \left\langle \sum_{m,n} \delta(\mathbf{r} - \mathbf{r}_m^{(j)}(t+\tau) + \mathbf{r}_n^{(k)}(t)) \right\rangle \Big/ \langle N_k \rangle \tag{A.3c}$$

The last identity (A.3c) holds only in the classical case where all position operators commute. It is often advantageous to consider the frequency components of the above systems. In order to avoid divergence for the limit of translation-invariant and thus infinite systems we consider the normalized Fourier transforms of the above quantities. The spectrum of the particle density is given by

$$\hat{C}_j(\mathbf{k}, t) = \int d^3 r \exp\left(i\mathbf{k}\mathbf{r}\right) C_j(\mathbf{r}, t) \Big/ V \tag{A.4a}$$

The Fourier transform of the density-density time correlation function is

$$\hat{H}_{jk}(\mathbf{k}, \mathbf{r}', \tau) = \int d^3 r \exp\left(i\mathbf{k}\mathbf{r}\right) H_{jk}(\mathbf{r}, \mathbf{r}', \tau) \Big/ V \tag{A.4b}$$

$$= \exp\left(-i\mathbf{r}'\mathbf{k}\right) \left\langle \hat{C}_j(\mathbf{k}, t) C_k(\mathbf{r}', t) \right\rangle \Big/ \langle C_k \rangle \tag{A.4c}$$

For $V \to \infty$ the volume average with respect to $\mathbf{r}'$ of equation (A.4c) becomes a Fourier transform and we can write

$$\hat{H}_{jk}(\mathbf{k}, \tau) = \left\langle \hat{C}_j(\mathbf{k}, t+\tau) \hat{C}_k^*(\mathbf{k}, t) \right\rangle \Big/ \langle C_k \rangle \tag{A.5}$$

This function is called the intermediate scattering function. The static structure factor of the liquid is simply given by

$$S_{jk}(\mathbf{k}) = \hat{H}_{jk}(\mathbf{k}, 0) \tag{A.6}$$

If a liquid is at equilibrium its dynamical properties manifest themselves in concentration fluctuations. In FCS theory one therefore usually considers the correlation functions of the fluctuations rather than the quantities defined above. However, both differ only by a constant and a scaling factor. For a system with translational invariance we have

$$\phi_{jk}(\mathbf{r}, \tau) = \left\langle \delta C_j(\mathbf{r}, t+\tau) \, \delta C_k(0, t) \right\rangle \tag{A.7}$$

And using $\langle \delta C \rangle = 0$ this can be expressed in terms of the van Hove function

$$\phi_{jk}(\mathbf{r}, \tau) = \langle C_k \rangle H_{jk}(\mathbf{r}, \tau) - \langle C_k \rangle \langle C_j \rangle \tag{A.8}$$

It is interesting to note that $\phi_{jk}/\langle C_k\rangle$ and $\langle C\rangle$ can be considered the 'self' and the 'distinct'-part of the van Hove function, the latter just being the probability per volume element to find an unrelated particle of type $j$. The 'self' part is the contribution due to possible movement of the particle originally at the origin to position $\mathbf{r}$ and, if $j \neq k$, its conversion during the time span $\tau$.

## A.2 Fluorescence Imaging Correlation Spectroscopy

The signal in both, FCS and FICS has the form of equation (3.9) but the two techniques use a different approach to extract information about $\hat{\phi}$ and hence the fluid. In FCS the correlation function $G$ is predicted by modelling the dynamic behaviors of the fluid theoretically. During experiments the model is tested for validity and its parameters are determined. FICS is the attempt to measure $\hat{\phi}$ directly in cases were a model for the dynamic structure under consideration is not available. This can be accomplished by choosing the PSFs in such a way that $G$ is dominated by the form of $\hat{\phi}$ at a single, adjustable frequency. It is clear from equation (3.9) that this implies sharp maxima of the OTF and therefore large focal areas. In principle FICS uses the fact that a large focal spot with a superimposed harmonic modulation probes the strength of a single Fourier component of an image. It is therefore restricted to samples which can be considered homogeneous over the portion illuminated by the pattern. While FICS has so far only been applied under the assumption of isotropic samples this limitation could be overcome by rotating the pattern.

The technique relies on a similar detection scheme as the frequency filtering method described in section 3.5. We assume the pattern to be strictly harmonic and therefore we only keep the first order of the effective PSF (3.52) and substitute it into equation (3.9). Assuming a single type of point-like, fluorescent particles and neglecting all constant factors, including the normalization with the average signal we obtain

$$G(\tau) = \int d^3k\, \hat{\phi}_{jk}(\mathbf{k}, \tau) \sum_{l,m=\pm 1} \exp(il\phi_1 + im\phi_2)$$
$$\times\, \hat{h}_e(\mathbf{k} - l\boldsymbol{\kappa}, t)\hat{h}_e(\mathbf{k} + m\boldsymbol{\kappa}, t + \tau) \quad \text{(A.9)}$$

Using the Gauss approximation (3.21) for the envelope and defining

$$a_\pm = [\mathbf{k} \pm \boldsymbol{\kappa}]^t \mathbf{A} [\mathbf{k} \pm \boldsymbol{\kappa}] \quad \text{(A.10)}$$

this becomes

$$G(\tau) = \pi^3 \det(\mathbf{A}) \int d^3k \hat{\phi}(\mathbf{k}, \tau) \Big[ \exp(-a_-/4) \exp(i\Delta\phi)$$
$$+ \exp(-a_+/4) \exp(-i\Delta\phi)$$
$$+ \exp(-[a_- + a_+]/8) \cos(i\phi_1 + i\phi_2) \Big]/8 \quad \text{(A.11)}$$

Effectively this is a convolution of $\hat{\phi}$ with a three dimensional Gauss peak evaluated at $\pm\boldsymbol{\kappa}$ plus a contribution from the last line that becomes small for sharp peaks. In the limit of very large envelopes we can use the identity (B.5) and obtain, again neglecting all constants

$$G(\tau) = \exp(i\Delta\phi)\hat{\phi}(\boldsymbol{\kappa}, \tau) + \exp(-i\Delta\phi)\hat{\phi}(-\boldsymbol{\kappa}, \tau) \quad \text{(A.12)}$$

Because the van Hove function is real we have

$$\hat{\phi}(-\mathbf{k}, \tau) = \hat{\phi}(\mathbf{k}, \tau)^* \quad \text{(A.13)}$$

and thus

$$G(\tau) = 2\Re\left[\exp(i\Delta\phi)\hat{\phi}(\boldsymbol{\kappa}, \tau)\right] \quad \text{(A.14)}$$

By recording two correlation curves $G_a$ and $G_x$ with $\Delta\phi = 0$ and $\Delta\phi = \pi/2$ for each vector $\boldsymbol{\kappa}$ real and imaginary part of $\hat{\phi}$ can be imaged separately:

$$G_a(\tau) = 2\Re\left[\hat{\phi}(\boldsymbol{\kappa}, \tau)\right] \quad \text{(A.15a)}$$
$$G_x(\tau) = 2\Im\left[\hat{\phi}(\boldsymbol{\kappa}, \tau)\right] \quad \text{(A.15b)}$$

We note that $\hat{\phi}$ contains both, information about movement and location of the particles in the fluid and their intrinsic dynamics, including reaction among them. In cases where these processes appear as a factor in $\hat{\phi}$ a comparison of patterned and unpatterned correlation curves can separate them from spatial information. In fact equation (3.54) reveals that in the limit of an infinite envelope and neglecting higher harmonics the directional correlation function is

$$\gamma \propto \exp\left(-4\tau\boldsymbol{\kappa}^t\mathbf{D}\boldsymbol{\kappa}\right)\cos\left(2\boldsymbol{\kappa}^t\mathbf{v} + \Delta\phi\right) = \Re\left[\hat{\alpha}(2\mathbf{k}, \tau)\exp(i\Delta\phi)\right] \quad \text{(A.16)}$$

and thus, instead of $\hat{\phi}$ only the portion corresponding to particle movement is determined.

# Appendix B

# Mathematical Appendix

## B.1 Integration Formulae

For the integration and Fourier transformation of the three-dimensional Gaussians in the analytical approximation for FCS the following generalization of the one-dimensional Gauss integral is needed. When applying the identity it should be kept in mind that the determinant is multi-linear in the lines and rows of a matrix and therefore in $n$-dimensional space we have $\det(x\mathbf{A}) = x^n \det(\mathbf{A})$ for any quadratic matrix $\mathbf{A}$.

**Lemma 1** *If $\mathbf{b}$ is an arbitrary complex vector and $\mathbf{A}$ is a real and symmetric matrix with positive eigenvalues $\nu_i^2$ then*

$$\mathcal{I} = \int d^3 s \exp\left(-\mathbf{s}^t \mathbf{A} \mathbf{s} + \mathbf{b}^t \mathbf{s}\right) = \sqrt{\pi^3 / \det(\mathbf{A})} \exp\left(\mathbf{b}^t \mathbf{A}^{-1} \mathbf{b} / 4\right) \qquad \text{(B.1)}$$

*Proof:* We start from the corresponding one-dimensional integral. For any $b \in \mathbb{C}$ and real $a > 0$ the identity

$$\int ds \exp\left(-as^2 + bs\right) = \sqrt{\pi/a} \exp\left(b^2/4a\right) \qquad \text{(B.2)}$$

can be readily verified using Cauchy's integral theorem and completing the square in the exponential's argument. However, because $\mathbf{A}$ is positive definite we can find an orthogonal matrix $\mathbf{O}$ with $\mathbf{A} = \mathbf{O}^t \mathbf{D} \mathbf{O}$ and the diagonal matrix given by $D_{ij} = \delta_{ij} \nu_i^2$. Rotating the coordinate system about $\mathbf{O}$ we obtain

$$\mathcal{I} = \int d^3 s \exp\left(-\mathbf{s}^t \mathbf{D} \mathbf{s} + \mathbf{b}^t \mathbf{O}^t \mathbf{s}\right) = \prod_i \int ds \exp\left(-\nu_i^2 s^2 + [\mathbf{O}\mathbf{b}]_i s\right) \qquad \text{(B.3)}$$

and applying equation (B.2) for each factor we obtain

$$\mathcal{I} = \sqrt{\pi^3}/(\nu_1\nu_2\nu_3) \exp\Big(\sum_i [\mathbf{Ob}]_i^2/4\nu_i^2\Big)$$

$$= \sqrt{\pi^3}/(\nu_1\nu_2\nu_3) \exp\Big(\mathbf{b}^t\mathbf{O}^t\mathbf{D}^{-1}\mathbf{Ob}/4\Big) \quad \text{(B.4)}$$

This proofs the above identity keeping in mind the definition of $\mathbf{A}$ and because $\det(\mathbf{O}) = 1$.

When making the transition from patterned FCS to FICS the Gauss peaks of the transfer function become sharper and effectively select a single spatial frequency of the van Hove function. Mathematically this process is described by the following

**Lemma 2** *Let $\mathbf{b}$ be an arbitrary complex vector and $\mathbf{A}$ be positive definite as above. If the function $f(\mathbf{s})$ is analytical the following identity holds:*

$$\lim_{\nu_i\to\infty} \det(\mathbf{A}) \int d^3s \exp\Big(-[\mathbf{s}-\mathbf{b}]^t\mathbf{A}[\mathbf{s}-\mathbf{b}]\Big) f(\mathbf{s}) = \sqrt{\pi^3}\, f(\mathbf{b}) \quad \text{(B.5)}$$

*Proof:* We start with the corresponding one-dimensional integral and a Gaussian located at the origin

$$a \int ds f(s) \exp\Big(-a^2 s^2\Big) = a \sum_{n=0}^{\infty} f^{(n)}(0) \int ds s^n \exp(-a^2 s^2)/n! \quad \text{(B.6)}$$

Due to symmetry only the contributions with even $n$ are nonzero and using substitution and partial integration we find

$$\int ds\, s^{2n}\exp(-a^2 s^2) = \Gamma(n+1/2)/a^{2n+1} \quad \text{(B.7)}$$

Thus equation (B.6) becomes

$$a \int ds f(s) \exp\Big(-a^2 s^2\Big) = a \sum_{n=0}^{\infty} \Gamma(n+1/2) f^{(n)}(0)/(n!\, a^{n+1}) \quad \text{(B.8)}$$

and finally in the limit $a \to \infty$ using $\Gamma(1/2) = \sqrt{\pi}$

$$\lim_{a\to\infty} a \int ds \exp\Big(-a^2 s^2\Big) f(s) = \sqrt{\pi}\, f(0) \quad \text{(B.9)}$$

In the multi-dimensional case we rotate and shift the coordinate system such that $\mathbf{A}$ is diagonal and $\mathbf{b}$ is zero. The one-dimensional argument can then be applied along each cartesian axis independently because $f$ is analytical, proving the lemma.

# Appendix C

# More Transfer Functions

## C.1 Extension of the Formalism

A confocal microscope in reflection mode can be characterized by its coherent transfer function (CTF). The theoretical description of such a microscope is not part of this discussion but the modifications to the previously developed formalism, which are needed in order to apply it to the CTF's calculation, shall be briefly addressed. The CTF contains products of two vector components $f$ and $g$ of the form $fg$[60], thus lacking the conjugation of the first factor. The correlation in equation $(2.6)$ is therefore substituted by a convolution:

$$\mathcal{F}[fg]\left(\mathbf{k}\right) = (2\pi)^3 \int d^3k' A_f\left(\mathbf{k}'\right) \delta\left(k'-1\right) A_g\left(\mathbf{k}-\mathbf{k}'\right) \delta\left(\left|\mathbf{k}-\mathbf{k}'\right|-1\right) \quad \text{(C.1)}$$

changing the geometry of our problem. If we redefine the vectors $\mathbf{k}_1 = \mathbf{k}'$ and $\mathbf{k}_2 = \mathbf{k} - \mathbf{k}'$ and use the same coordinate transformation as above we obtain

$$\mathcal{F}[fg]\left(\mathbf{k}\right) = (2\pi)^3 \int d\varphi'' A_f\left(\mathbf{k}_1\right) A_g\left(\mathbf{k}_2\right)/k \Bigg|_{\cos\vartheta''=k/2, k''=1} \quad \text{(C.2)}$$

Using equation $(2.7)$, we find the Cartesian components of the new vectors $\mathbf{k}_1$ and $\mathbf{k}_2$ to be

$$m_{1/2} = (b \pm a)\cos\varphi \mp d\sin\varphi \quad \text{(C.3a)}$$

$$n_{1/2} = (b \pm a)\sin\varphi \pm d\cos\varphi \quad \text{(C.3b)}$$

$$s_{1/2} = \mp r_0 \sin\vartheta \cos\varphi'' + (k\cos\vartheta)/2 \quad \text{(C.3c)}$$

The integration range is now defined by $-s_{1/2} \geq \cos\alpha$, resulting in

$$\beta_2 \leq |\phi''| \leq \pi - \beta_2$$

$$\beta_2 = \arccos\left[(-k\cos\vartheta - 2\cos\alpha)/(2r_0\sin\vartheta)\right] \quad \text{(C.4)}$$

If the argument of the inverse cosine is larger than 1 or smaller than zero, we have $\beta_2 = 0$ and $\beta_2 = \pi/2$ respectively. Depending on the desired observables one can now go on to substitute equations (C.3) and (2.12) into (C.2) and extract the angular dependence in analogy to (2.14).

# References

[1] D. Magde, E.L. Elson, and W.W. Webb. Thermodynamic fluctuations in a reacting system - measurement by fluorescence correlation spectroscopy. *Phys. Rev. Lett.*, 29(11):705–708, 1972. 6, 29

[2] T. Ha, Th. Enderle, D.S. Chemla, and S. Weiss. Dual-molecule spectroscopy: Molecular rulers for the study of biological macromolecules. *IEEE J. Select. Top. Quantum Electron.*, 2(4):1115–1128, 1996. 6

[3] I. Majoul, M. Straub, R. Duden, S. W. Hell, and H.D. Söling. Fluorescence resonance energy transfer analysis of protein-protein interactions in single living cells by multifocal multiphoton microscopy. *Rev. Mol. Biotechn.*, 82:267–277, 2002. 6

[4] E. Abbe. Beiträge zur Theorie des Mikroskops und der Mikroskopischen Wahrnehmung. *Arch. f. Mikroskop. Anat.*, 9:413–420, 1873. 6

[5] C.J.R. Sheppard, G. Calvert, and M. Wheatland. Focal distribution for superresolving toraldo filters. *J. Opt. Soc. Am. A*, 15(4):849–856, 1998. 6

[6] C.M. Blanca, J. Bewersdorf, and S.W. Hell. Single sharp spot in fluorescence microscopy of two opposing lenses. *Appl. Phys. Lett.*, 79(15):2321–2323, 2001. 7

[7] C.M. Blanca and S.W. Hell. Sharp spherical focal spot by dark ring 4Pi-confocal microscopy. *Single Mol.*, 2(3):207–210, 2001. 7

[8] S.W. Hell, M. Schrader, M. Nagorni, and H. T. M. van der Voort. 4Pi-confocal microscopy restored with the 4Pi-psf provides 3d-resolution in the 100 nm range. *Cell Vision -J. Anal. Morphol.*, 4(2):187, 1997. 7

[9] S.W. Hell, P.E. Hänninen, M. Schrader, T. Wilson, and E. Soini. Resolution

beyond the diffraction limit: 4Pi-confocal, STED, and GSD. *Zool. Stud.*, 34:Suppl. I, 70, 1995.  7

[10] A. Schönle, P.E. Hänninen, and S.W. Hell. Nonlinear fluorescence through intermolecular energy transfer and resolution increase in fluorescence microscopy. *Ann. Phys. (Leipzig)*, 8(2):115–133, 1999.  7

[11] A. Schönle and S. W. Hell. Far-field fluorescence microscopy with repetetive excitation. *Eur. Phys. J. D*, 6:283–290, 1999.  7

[12] M. Dyba. *Spektroskopische Anwendungen der STED-Mikroskopie*. Diploma thesis, Max-Planck-Institute for biophysical Chemistry and Ruprecht-Karls-Universität, 2000.  7

[13] M. Dyba and S.W. Hell. Focal spots of size l/23 open up far-field fluorescence microscopy at 33 nm axial resolution. *Phys. Rev. Lett.*, 88:163901, 2002.  7

[14] T. A. Klar, S. Jakobs, M. Dyba, A. Egner, and S. W. Hell. Fluorescence microscopy with diffraction resolution limit broken by stimulated emission. *Proc. Natl. Acad. Sci. USA*, 97:8206–8210, 2000.  7

[15] E. Wolf. Three-dimensional structure determination of semi-transparent objects from holographic data. *Opt. Commun.*, 1(4):153, 1969.  9

[16] C. W. McCutchen. Generalized aperture and the three-dimensional diffraction image. *J. Opt. Soc. Am.*, 54:240–244, 1964.  9

[17] B. R. Frieden. Optical transfer of a three-dimensional object. *J. Opt. Soc. Am.*, 57:56–66, 1967.  9, 10

[18] C. J. R. Sheppard, M. Gu, Y. Kawata, and S. Kawata. Three-dimensional transfer functions for high-aperture systems. *J. Opt. Soc. Am. A*, 11(2):593–596, 1993.  9, 10

[19] A. Schönle and S. W. Hell. Heating by absorption in the focus of an objective lens. *Opt. Lett.*, 23(5):325–327, 1998.  9

[20] H. H. Hopkins. Resolving power of the microscope using polarized light. *Nature*, 155:275, 1945.  9

[21] V. S. Ignatowsky. Diffraction by a lens having arbitrary opening. *Trans. Opt. Inst. Petrograd*, I:paper 4, 1919.  9

[22] E. Wolf. Electromagnetic diffraction in optical systems I. An integral representation of the image field. *Proc. R. Soc. A*, 253:349–357, 1959. 9

[23] B. Richards and E. Wolf. Electromagnetic diffraction in optical systems II. Structure of the image field in an aplanatic system. *Proc. R. Soc. Lond. A*, 253:358–379, 1959. 10, 11, 41

[24] C. J. R. Sheppard and K. G. Larkin. Vectorial pupil functions and vectorial transfer functions. *Optik*, 107(2):79–87, 1997. 10

[25] S.W. Hell, G. Reiner, C. Cremer, and E.H.K. Stelzer. Aberrations in confocal fluorescence microscopy induced by mismatches in refractive index. *J. Microsc.*, 169:391–405, 1993. 15

[26] P. Török, P. Varga, Z. Laczik, and G. R. Booker. Electromagnetic diffraction of light focused through a planar interface between materials of mismatched refraction indices: an integral representation. *J. Opt. Soc. Am. A*, 12(2):325–332, 1995. 15, 16

[27] Alexander Egner. *Punktabbildungsfunktion von Objektiven hoher Apertur beim Fokussieren durch eine Grenzschicht.* diploma thesis, Heidelberg, 1997. 19

[28] A. Egner, M. Schrader, and S. W. Hell. Refractive index mismatch induced intensity and phase variations in fluorescence confocal, multiphoton and 4Pi-microscopy. *Opt. Commun.*, 153:211–217, 1998. 19, 22

[29] K. Svoboda and S. M. Block. Biological applications of optical forces. *Annual Review of Biophysics Biomolecular Structure*, 23:247–85, 1994. 23

[30] W. Denk, D.W. Piston, and W.W. Webb. Two-photon molecular exciation in laser-scanning microscopy. In J.B. Pawley, editor, *Handbook of Biological Confocal Microscopy*, pages 445–458. Plenum Press, New York, 1995. 23

[31] Y. Liu, D. K. Cheng, G. J. Sonek, M. W. Berns, C. F. Chapman, and B. J. Tromberg. Evidence for localized cell heating induced by optical tweezers. *Biophys. J.*, 68:2137–2144, 1995. 23

[32] A. Sennaroglu. Quantitative study of laser beam probagation in a thermally loaded absorber. *J. Opt. Soc. Am. B*, 14(2):356–363, 1997. 23

[33] A. Gennerich and D. Schild. Fluorescence correlation spectroscopy in small cytosolic compartments depends critically on the diffusion model used. *Biophys. J.*, 79:3294–3306, 2000. 29

[34] A. Gennerich and D. Schild. Anisotropic diffusion in mitral cell dendrites revealed by fluorescence correlation spectroscopy. *Biophys. J.*, 83:510–522, 2002. 29, 72

[35] H. Asai and T. Ando. Fluorescence correlation spectroscopy illuminated by standing exciting waves. *J. Phys. Soc. Japan*, 40(5):1527–1528, 1976. 29

[36] P.-F. Lenne, E. Etienne, and H. Rigneault. Subwavelength patterns and high detection efficiency in fluorescence correlation spectroscopy using photonic structures. *Appl. Phys. Lett.*, 80(22):4106–4108, 2002. 30

[37] S.K. Davis and C.J. Bardeen. Using two-photon standing waves and patterned photobleaching to measure diffusion from nanometers to microns in biological systems. *Rev. Sci. Instrum.*, 73(5):2128–2135, 2002. 30

[38] R.L. Hansen, X. Ron Zhu, and J.M. Harris. Fluorescence correlation spectroscopy with patterned photoexcitation for measuring solution diffusion coefficients of robust fluorophores. *Anal. Chem.*, 70:1281–1287, 1998. 30, 44

[39] M Hattori, S Hideaki, and H Yokoyama. Fluorescence correlation spectroscopy with traveling interference fringe excitation. *Rev. Sci. Instrum.*, 67(12):4064–4071, 1996. 30, 44

[40] M.K. Knowles, T.J. Grassman, and A.H. Marcus. Measurement of the dynamic structure function of fluorescently labeled complex fluids by fourier imaging correlation spectroscopy. *Phys. Rev. Lett.*, 85(13):2837–2840, 2000. 30

[41] J. Widengren, R. Rigler, and Ü. Mets. Triplet-state monitoring by fluorescence correlation spectroscopy. *J. Fluorescence*, 4:255–258, 1994. 33

[42] K. Schätzel. Noise on photon correlation data: I. autocorrelation functions. *Ouantum Opt.*, 2:287–305, 1990. 39, 51

[43] S. Hell and E. H. K. Stelzer. Properties of a 4Pi-confocal fluorescence microscope. *J. Opt. Soc. Am. A*, 9:2159–2166, 1992. 41

[44] A. Egner, S. Jakobs, and S.W. Hell. Fast 100-nm resolution 3d-microscope reveals structural plasticity of mitochondria in live yeast. *Proc. Natl. Acad. Sci. USA*, 99:3370–3375, 2002.   45

[45] J. Bewersdorf, R. Pick, and S. W. Hell. Multifocal multiphoton microscopy. *Opt. Lett.*, 23:655–657, 1998.   45

[46] T. Wohland, R. Rigler, and H. Vogel. The standard deviation in fluorescence correlation spectroscopy. *Biophys. J.*, 80:2987–2999, 2001.   46, 51

[47] K. Starchev, J. Zhang, and J. Buffle. Applications of fluorescence correlation spectroscopy - particle size effect. *J. Colloid Interface Sci.*, 203:189–196, 1998.   46, 51

[48] W. H. Press, B. P. Flannery, S. A. Teukolsky, and W. T. Vetterling. *Numerical Recipes in C*. Cambridge University Press, 2 edition, 1993.   47, 51

[49] J.A. Nelder and R. Mead. A simplex method for function minimization. *Computer Journal*, 7:308–313, 1965.   48

[50] K. Schätzel, M. Drewel, and S. Stimac. Photon correlation measurements at large lag times: improving statistical accuracy. *J. Mod. Opt.*, 35(4):711–718, 1987.   51

[51] P. Kask, R. Günther, and P. Axhausen. Statistical accuracy in fluorescence fluctuation experiments. *Eur. Biophys. J.*, 25:163–169, 1996.   51

[52] D. E. Koppel. Statistical accuracy in fluorescence correlation spectroscopy. *Phys. Rev. A*, 10(6):1938.1945, 1974.   51

[53] H. Quian. On the statistics of fluorescence correlation spectroscopy. *Biophys. Chem.*, 38:49–57, 1990.   51

[54] Kurt Sätzler and Roland Eils. Resolution improvement by 3-d reconstructions from tilted views in axial tomography and confocal theta microscopy. *Bioimaging*, 5(4):171–182, 1997.   53

[55] M. Dyba, T. A. Klar, S. Jakobs, and S. W. Hell. Ultrafast dynamics microscopy. *Appl. Phys. Lett.*, 77:597–599, 2000.   60

[56] Th. Förster. Zwischenmolekulare Energiewanderung und Fluoreszenz. *Annalen der Physik*, 2:55–75, 1948.   61

[57] A.A. Deniz, M. Dahan, J.R. Grunwell, T. Ha, A.E. Faulhaber, D.S. Chemla, S. Weiss, and P.G. Schultz. Single-pair fluorescence resonance energy transfer on freely diffusion molecules: Observation of förster distance dependence and subpopulations. *Proc. Natl. Acad. Sci. USA*, 96:3670–3675, 1999.  61, 63, 68

[58] M. Schrader, F. Meinecke, K. Bahlmann, M. Kroug, C. Cremer, E. Soini, and S.W. Hell. Monitoring the excited state of a dye in a microscope by stimulated emission. *Bioimaging*, 3:147–153, 1995.  64

[59] A. Schönle, M. Glatz, and S. W. Hell. Four-dimensional multiphoton microscopy with time-correlated single-photon counting. *Appl. Optics*, 39(34):6306–6311, 2000.  67

[60] C. J. R. Sheppard, M. Gu, and X. Q. Mao. Three-dimensional coherent transfer function in a reflection-mode confocal scanning microscope. *Opt. Commun.*, 81:281–284, 1991.  79

# Acknowledgements

# Publications Resulting from this Thesis

A. Schönle and S.W. Hell. *Heating by absorption in the focus of an objective lens.* Opt. Lett., 23(5):325-327, 1998.

A. Schönle, M.Glatz, and S.W. Hell. *Four-dimensional multiphoton microscopy with time-correlated single-photon counting.* Appl. Optics, 39(34):6306-6311, 2000.

S. Jakobs, V. Subramanian, A. Schönle, T.M. Jovin, and S.W. Hell. *EGFP and DsRed expressing cultures of escherichia coli imaged by confocal, two-photon and fluorescence lifetime microscopy.* FEBS Lett., 479(3):131–135, 2000.

A. Schönle and S.W. Hell. *Calculation of vectorial three-dimensional transfer functions in large-angle focusing systems.* J. Opt. Soc. Am. A, 19(10):2121-2126, 2002.